Chemical Mapping of Temperate Sub-Neptune Atmospheres: Constraining the Deep Interior H_2O/H_2 Ratio from the Atmospheric CO_2/CH_4 Ratio

Jeehyun Yang[1] and Renyu Hu[1,2]

[1] Jet Propulsion Laboratory, California Institute of Technology, Pasadena, CA 91109, USA; jeehyun.yang@jpl.nasa.gov
[2] Division of Geological and Planetary Sciences, California Institute of Technology, Pasadena, CA 91125, USA; renyu.hu@jpl.nasa.gov
Received 2024 June 1; revised 2024 July 23; accepted 2024 July 28; published 2024 August 19

Abstract

Understanding the planetary envelope composition of sub-Neptune-type exoplanets is challenging due to the inherent degeneracy in their interior composition scenarios. Particularly, the planetary envelope's H_2O/H_2 ratio, which can also be expressed as the O/H ratio, provides crucial insights into its original location relative to the ice line during planetary formation. Using self-consistent radiative transfer modeling and a rate-based automatic chemical network generator combined with 1D photochemical kinetic-transport atmospheric modeling, we investigate various atmospheric scenarios of temperate sub-Neptunes, ranging from H_2-dominated to H_2O-dominated atmospheres with equilibrium temperatures (T_{eq}) of 250—400 K. This study includes examples such as K2-18 b ($T_{eq} = 255$ K), LP 791-18 c ($T_{eq} = 324$ K), and TOI-270 d ($T_{eq} = 354$ K). Our models indicate that the atmospheric CO_2/CH_4 ratio can be used to infer the deep interior H_2O/H_2 ratio. Applying this method to recent JWST observations, our findings suggest that K2-18 b likely has an interior that is 50% highly enriched in water, exceeding the water content in a $100 \times Z_\odot$ scenario and suggesting a planetary formation mechanism involving substantial accretion of ices. In contrast, our model suggests that approximately 25% of TOI-270 d's interior is composed of H_2O, which aligns with the conventional metallicity framework with a metallicity higher than $100 \times Z_\odot$. Furthermore, our models identify carbonyl sulfide (OCS) and sulfur dioxide (SO_2) as strong indicators for temperate sub-Neptunes with at least 10% of their interior composed of water. These results provide a method to delineate the internal composition and formation mechanisms of temperate sub-Neptunes ($T_{eq} < \sim 500$ K) via atmospheric characterization through transmission spectroscopy.

Unified Astronomy Thesaurus concepts: Astrochemistry (75); Exoplanet atmospheres (487); Planet formation (1241); Exoplanet formation (492); Theoretical models (2107); Exoplanet atmospheric composition (2021); James Webb Space Telescope (2291); Mini Neptunes (1063)

1. Introduction

Sub-Neptune-sized planets separated from super-Earth-sized planets by the radius valley near $1.8\,R_\oplus$ generally have a volatile-rich envelope and are the most common types of planets detected so far (Fulton et al. 2017; Fulton & Petigura 2018; Van Eylen et al. 2018; Hardegree-Ullman et al. 2019). Despite their prevalence, our understanding of the interior composition of sub-Neptunes is very limited due to the inherent degeneracy in their interior structure composition. The radius and mass of sub-Neptunes can be explained by either (i) a massive, high-molecular-weight (e.g., H_2O) volatile layer or (ii) a lighter H_2/He-dominated envelope on top of a rock/iron core (Rogers & Seager 2010; Valencia et al. 2010; Luque & Pallé 2022).

For this reason, precise characterization of the internal composition and resulting chemistry of sub-Neptunes has become increasingly important from a formation and evolution perspective. This characterization might help distinguish between different pathways of sub-Neptune formation. For example, "H_2O-rich" sub-Neptunes are believed to form farther from their star, beyond the ice line, where they can efficiently accrete large amounts of water and volatiles in the form of solid material before migrating to their current close-in orbits

(Lambrechts et al. 2014; Morbidelli et al. 2015; Venturini et al. 2020). In contrast, "H_2-rich" sub-Neptunes with lower volatile content are thought to originate within the ice line, where volatiles are not present as ice, and most of their mass is accumulated through the accretion of drifting rocky pebbles (Johansen & Lambrechts 2017). Therefore, determining the deep interior H_2O/H_2 ratio of sub-Neptunes spanning the radius valley is essential for enhancing our understanding of planetary formation and evolution.

Temperate sub-Neptunes ($200\,K \leqslant T_{eq} \leqslant 400\,K$) are excellent targets for studying planetary interior compositions using JWST observations. Cold exoplanets could potentially have liquid water oceans (note that Earth has $T_{eq} \sim 255\,K$, and has oceans), leading to atmospheric compositions primarily regulated by interactions with liquid water. As a result, atmospheric composition does not directly represent the envelope composition (e.g., gaseous ammonia is highly soluble in liquid water, which leads to depletion in the upper atmosphere). On the other hand, many hotter exoplanets are predicted to contain carbon monoxide (CO) and CO_2 in their atmospheres due to their higher thermochemical stability compared to CH_4 at high temperatures, and thus these gases do not exclusively represent the deep interior composition (Line et al. 2011; Moses et al. 2011, 2016; Venot et al. 2012; Tsai et al. 2018; Fortney et al. 2020). Additionally, studies have shown that exoplanets with T_{eq} between 500 and 800 K exhibit the most attenuated spectral features, likely due to thick clouds and hazes (Morley et al. 2015; Brande et al. 2024).

Therefore, temperate sub-Neptunes with T_{eq} lower than 400 K are favorable observation targets. However, it is important to note that water may condense below the photosphere (the region probed by JWST) in the cooler end of the temperate range (i.e., $T_{eq} \sim 250$ K), complicating the direct inference of internal H_2O content from atmospheric observations. Recent advancements in observational techniques with high enough signal-to-noise ratios have made sub-Neptunes favorable targets as well. Numerous JWST observations of various sub-Neptunes are already available, such as K2-18 b (Madhusudhan et al. 2023) and TOI-270 d (Benneke et al. 2024), or will be available soon (LP 791-18 c). Since high-altitude clouds or hazes that form at $T_{eq} \leqslant 400$ K are unlikely to obscure the transmission spectra (Morley et al. 2015), JWST observations can provide detailed and valuable information about the molecular species present in these atmospheres.

Several efforts have been made to infer the elemental composition of the deep atmospheres of sub-Neptunes using both theoretical and observational studies (Thorngren et al. 2016; Thorngren & Fortney 2019; Luque & Pallé 2022; Benneke et al. 2024; Burn et al. 2024). A previous study has modeled the atmospheres of water-rich sub-Neptunes (from solar abundance to 100% H_2O) using 1D radiative–convective equilibrium modeling coupled with their associated transmission and thermal emission spectra (Kempton et al. 2023). However, this approach lacks disequilibrium chemistry and thus may miss infrared absorbers beyond those abundant in thermochemical equilibrium. To our knowledge, no attempts have been made to infer the envelope composition, particularly the H_2O/H_2 ratio of potential water-rich temperate sub-Neptunes, by fully utilizing 1D photochemical modeling. CO_2 is a carbon-bearing species indicative of high temperatures and oxidative atmospheres, while CH_4 indicates low temperatures and reducing atmospheres (Moses et al. 2011, 2016). Consequently, the ratio between these two molecules can provide insights into the bulk envelope H_2O/H_2 ratio of temperate sub-Neptunes, potentially helping us understand their original locations relative to the ice line within the protoplanetary disk (Johansen & Lambrechts 2017; Burn et al. 2024).

In this work, we employ self-consistent radiative transfer modeling and a state-of-the-art rate-based automatic chemical network generator combined with 1D photochemical kinetic-transport atmospheric modeling to investigate various atmospheric scenarios ranging from H_2-dominated (representing gas accretion) to H_2O-dominated (representing ice accretion) atmospheres of temperate sub-Neptune-type exoplanets. We introduce a new method for inferring the deep interior (or bulk envelope) H_2O/H_2 ratio from the atmospheric CO_2/CH_4 ratio and a new framework to classify temperate sub-Neptunes using this O/H ratio, different from the conventional multipliers of the solar metallicity framework (i.e., $n \times Z_\odot$). This new variable (i.e., O/H ratio) not only guides the interpretation of JWST observations of sub-Neptunes but also provides new insights into their original location within the protoplanetary disk during planetary formation.

2. Methods

2.1. Elemental Parameterization of Planetary Envelope Accretion

To investigate the diverse envelope accretion scenarios of sub-Neptunes, we established seven distinct H_2O/H_2 accretion scenarios, represented by corresponding oxygen-to-hydrogen (O/H) ratio scenarios, ranging from H_2-rich to H_2O-rich

envelopes. This variability was numerically achieved by adjusting the O/H ratio beyond the framework of conventional solar metallicity, $Z_\odot$ (Lodders 2020). As detailed in Table A1 in Appendix A, the third column lists standard multipliers of solar metallicity ($Z_\odot$) at $1\times$, $10\times$, $100\times$, $1000\times$, and $10,000\times$ (denoted as H_2:H_2O accretion ratio = 100:0 for simplicity). Based on this and while retaining the original abundances of carbon, nitrogen, and sulfur (i.e., each elemental abundance follows its solar elemental abundance multiplied by an integer, n), we systematically varied the O-to-H ratio according to the equations detailed in Appendix A. From now on, maintaining C, N, and S at each of their solar elemental abundances multiplied by n is denoted as $[C + N + S] = n \times Z_\odot$.

This spectrum of accretion scenarios (see the description of x_{acc} in Appendix A) reflects the variations in planetary formation locations, particularly concerning the ice line, as depicted in Figure A1 in Appendix A. Overall, we analyzed 74 planetary atmospheric structures (temperature–pressure, T–P, profiles) and 80 planetary atmospheric photochemical models, the details of which are described in Appendix A.

2.2. The T–P Profiles for Various Planetary Envelope Accretion Scenarios

For each of the elemental parameterizations of planetary envelope accretion mentioned in Section 2.1, we calculated 74 T–P profiles under radiative–convective equilibrium using the climate module of the ExoPlanet Atmospheric Chemistry and Radiative Interaction Simulator (EPACRIS-Climate; M. Scheucher et al. 2024, in preparation), and the results are presented in Figure B1 in Appendix B ($1000\times$ and $10,000\times$ solar metallicity cases for K2-18 b are omitted for simplicity). Further details on this radiative–convective equilibrium modeling can be found in Appendix B.

2.3. Automatic Chemical Reaction Network Generation for H_2O-rich Chemistry

A detailed chemical reaction network for H_2O-rich atmospheres was constructed using the Reaction Mechanism Generator (RMG; Gao et al. 2016; Johnson et al. 2022), a Python-based open-source software. RMG generates chemical networks using a rate-based iteration algorithm and has been extensively described in previous literature (Gao et al. 2016; Liu et al. 2021). This method's application to exoplanet atmospheric studies is detailed in Yang & Hu (2024), and further details on this chemical reaction network generation for H_2O-rich chemistry can be found in Appendix C.

The final photochemical network comprised 92 species (56 originally available in the EPACRIS species and 36 species newly generated by RMG not available in the EPACRIS library, as listed in Table C1 in Appendix C). The network included 2009 reactions (343 original EPACRIS reactions = 40 photochemistry reactions + 248 bimolecular reactions + 34 termolecular reactions + 21 thermodissociation reactions, and 1666 reactions newly generated by RMG). Except for the 40 photochemistry reactions, the other 1969 reactions are forward–reverse reaction pairs. This comprehensive network was used in 1D photochemical kinetic-transport atmospheric modeling of various temperate sub-Neptune atmospheres, as described in Section 2.4.

2.4. 1D Photochemical Kinetic-transport Atmospheric Modelings

Based on the elemental scenarios outlined in Section 2.1, the T–P profiles calculated in Section 2.2, and the chemical network tailored for water-rich systems in Section 2.3, we performed 1D photochemical kinetic-transport atmospheric modeling of the 80 scenarios using the chemistry module of EPACRIS (Yang & Hu 2024). This modeling was conducted to simulate the steady-state vertical mixing ratios of chemical species in various atmospheric scenarios of temperate sub-Neptunes. Further details on the eddy diffusion coefficients and the stellar fluxes used in this study can be found in Appendix D.

After the models had converged and reached the steady state, we computed the synthetic transmission spectra of K2-18 b and TOI-270 d based on the molecular mixing ratio profiles using the transmission spectrum generation module of EPACRIS (Hu et al. 2013) and compared the resulting transmission spectra with published JWST observations (Madhusudhan et al. 2023; Benneke et al. 2024).

3. Results and Discussions

3.1. Constraining the Bulk Envelope H_2O/H_2 Ratio

3.1.1. Using the CO_2/CH_4 Ratio as a Constraint on the H_2O/H_2 Ratio

Figure 1 displays the upper atmospheric CO_2/CH_4 ratios plotted against the deep interior H_2O/H_2 ratios for various planetary envelope accretion scenarios, as detailed in Section 2.1. As an example, for the case of $H_2:H_2O = 50:50$ and the $[C + N + S] = 100\times$ solar metallicity scenario of K2-18 b, as illustrated in the left panel of Figure 4, we determined the CO_2 (red) and CH_4 (green) mixing ratios within the pressure range of 0.1–2 mbar, located within the gray shaded area, to derive the upper atmospheric CO_2/CH_4 ratios. Similarly, we obtained the H_2O (blue) and H_2 (black) mixing ratios at a pressure of 200 bars (i.e., 2×10^5 mbar) at the bottom to derive the deep interior H_2O/H_2 ratios. This approach allowed us to explore the relationship between the upper atmospheric CO_2/CH_4 ratios and the deep interior H_2O/H_2 ratios across various planetary envelope accretion scenarios. By analyzing these upper atmospheric CO_2/CH_4 ratios and comparing them to the CO_2/CH_4 ratios retrieved from the JWST observation of K2-18 b (Madhusudhan et al. 2023) and TOI-270 d (Benneke et al. 2024), we can further constrain the deep interior H_2O/H_2 ratio of each planet, respectively.

In general, as expected, we can see a clear consistent linear pattern across all planetary envelope accretion scenarios with more than 25% water (corresponding to $223 \times Z_\odot$, shown by a gray dotted line in Figure 1). This is because a H_2O-rich envelope creates an oxidative atmosphere favorable for CO_2 formation over CH_4, thus increasing the CO_2/CH_4 ratio as the H_2O content inside the planetary envelope increases. By leveraging this trend, we can effectively constrain the deep interior H_2O/H_2 ratio using the upper atmospheric CO_2/CH_4 ratio.

First, in the case of K2-18 b, as depicted in Figure 1, assuming $A_b = 0.3$ (i.e., $T_{eq} = 255$ K), an intrinsic temperature (i.e., T_{int}) of 60 K, and an eddy diffusion coefficient of 10^6 [cm^2 s^{-1}], the thicker blue shaded area represents the deep interior H_2O/H_2 constraints for K2-18 b, which range from ~25% to ~90% water-rich scenarios. This indicates that K2-18 b's envelope contains at least ~25% water. This statement

contrasts with the observations by Madhusudhan et al. (2023), which did not detect significant contributions from H_2O and thus did not provide any atmospheric retrievals on O/H ratios. As discussed later in Section 3.2, in the case of K2-18 b, its low equilibrium temperature of 255 K causes water to condense out at $P \sim 10^2$ mbar, making water detection challenging for JWST observations (see blue line in the left panel of Figure 4 and the upper panel of Figure 5). This underscores the importance of accurately addressing water condensation in atmospheric modeling to extract hidden information.

Adjusting for $T_{int} = 100$ K, to account for the sensitivity of the intrinsic temperature to the upper atmospheric CO_2/CH_4 ratios due to changes in deep interior T–P structure, the lighter blue shaded area now also marginally includes the conventional $100\times$ solar metallicity scenario, as denoted as blue hexagrams in Figure 1. This behavior is primarily attributed to elevated temperatures in the deep interior of K2-18 b, which favor the formation of CO_2 over CH_4 (Moses et al. 2011), thus elevating the upper atmospheric CO_2/CH_4 ratios in H_2-rich cases (e.g., $100\times$ solar metallicity) to align with the lower end of the JWST observational constraints on the CO_2/CH_4 ratio.

This elevated CO_2/CH_4 ratio in H_2-rich envelopes is also consistent with the modeling result of Wogan et al. (2024), which utilized a T–P profile that is ~150 K higher at 200 bars compared to the T–P profile computed by EPACRIS assuming the same T_{int} of 60 K. However, it is 100 K lower compared to the T–P profile computed by EPACRIS assuming a T_{int} of 100 K, which encompasses the uncertainty. Although the CO_2/CH_4 ratio predicted by Wogan et al. (2024) is slightly below the lower end of the JWST observational constraints on the CO_2/CH_4 ratio (see black cross in Figure 1), the synthesized transmission spectrum contained both CO_2 and CH_4 features. To determine whether the elevated CO_2/CH_4 ratios in the upper atmosphere of the H_2-rich case are predominantly due to the T–P profile rather than differences in the chemical networks used, we conducted photochemical modeling of the K2-18 b atmosphere. We used the same old $100\times$ solar metallicity from Lodders et al. (2009), where C/O = 0.46, compared to the recently updated value of C/O = 0.55 from Lodders (2020). We also applied the same T–P profile as in Wogan et al. (2024). The resulting CO_2/CH_4 ratio is denoted by a blue cross in Figure 1 and exhibits an almost identical value to that modeled by Wogan et al. (2024; see black cross). This emphasizes that accurate prediction of the interior T–P structure is crucial for using the upper atmospheric CO_2/CH_4 ratio to infer the deep interior H_2O/H_2 ratios.

We also tested the sensitivity of the eddy diffusion coefficients to the upper atmospheric CO_2/CH_4 ratios for the $H_2:H_2O = 50:50$ and $[C + N + S] = 100\times$ solar metallicity scenario of K2-18 b, denoted by upward- (assuming 10^8 [cm^2 s^{-1}]) and downward-pointing blue triangles (10^4 [cm^2 s^{-1}]) in Figure 1, which shows relatively less sensitivity compared to the sensitivity driven by varying intrinsic temperatures.

In the case of TOI-270 d, as depicted in Figure 1, assuming $A_b = 0$ (i.e., $T_{eq} = 387$ K), an intrinsic temperature (i.e., T_{int}) of 60 K, and an eddy diffusion coefficient of 10^6 [cm^2 s^{-1}], the magenta shaded area represents the deep interior H_2O/H_2 constraints for TOI-270 d, which indicates that TOI-270 d's envelope contains approximately 15%–25% water. These constraints align well with the quenched-chemistry atmospheric retrievals on O/H ratios (i.e., horizontal error bars in Figure 1) of the deep atmospheres (1–10 bars) based on the JWST
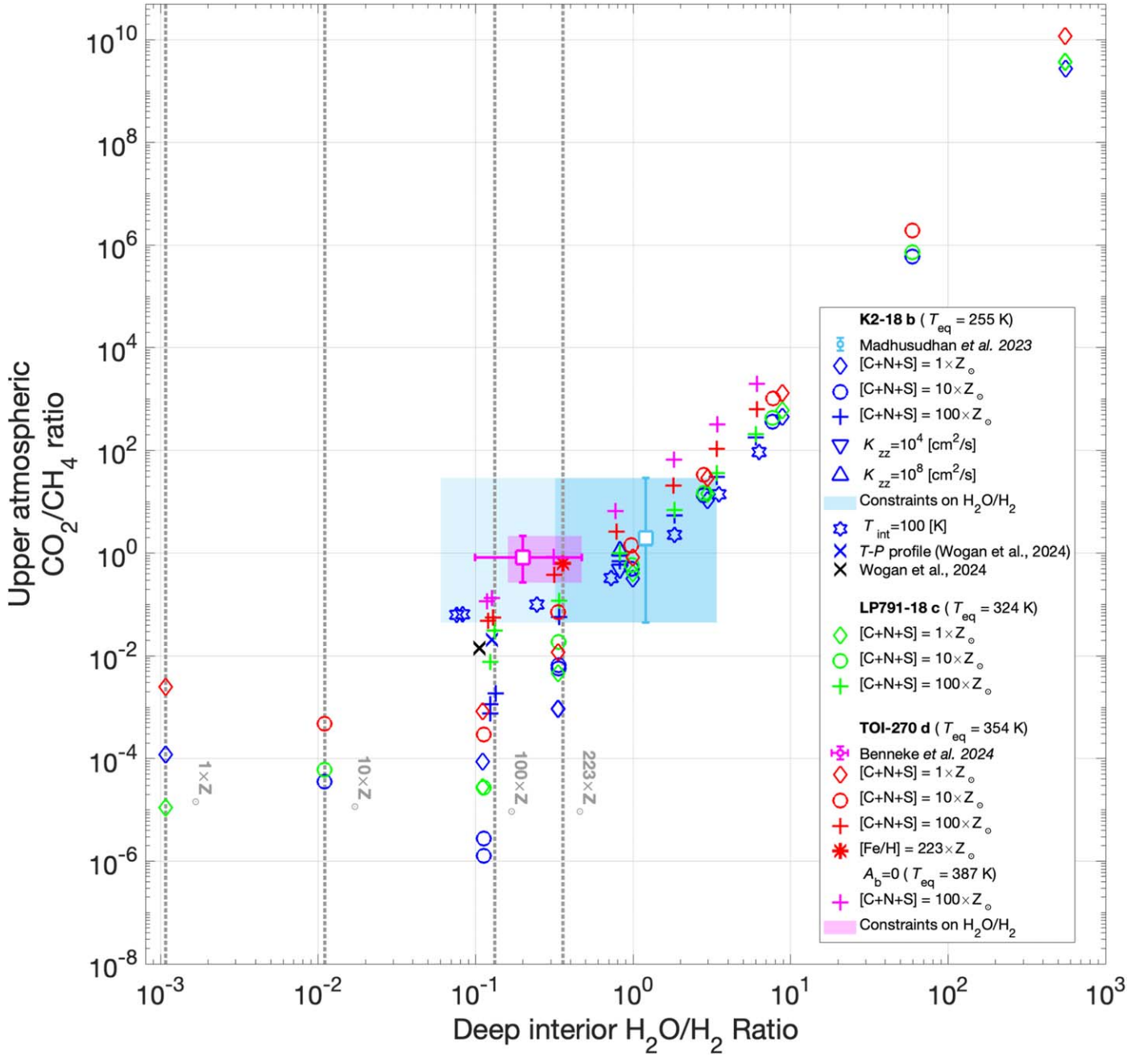
Figure 1. The figure shows the upper atmospheric ($P = 0.1–2$ mbar, corresponding to the JWST's primary probing range; Rustamkulov et al. 2023) CO_2-to-CH_4 ratios plotted against the deep interior ($P = 200$ bars) H_2O-to-H_2 ratios. Unless otherwise noted, the planetary equilibrium temperature (i.e., T_{eq}) is assumed based on $A_b = 0.3$ and an intrinsic temperature (T_{int}) of 60 K, with $Z_\odot$ denoting solar metallicity. The symbols in the figure represent different elemental parameterizations for the planetary envelope accretion scenarios. Diamonds indicate seven O/H scenarios (i.e., H_2:H_2O from 100:0 to 0:100) with elemental compositions of carbon, nitrogen, and sulfur ([C + N + S]) of $1 \times Z_\odot$. Circles represent the same O/H ratios but with [C + N + S] of $10 \times Z_\odot$, while plus signs correspond to $100 \times Z_\odot$. Upward- and downward-pointing triangles indicate the scenario with an H_2:H_2O ratio of 50:50 and [C + N + S] of $100 \times Z_\odot$ but assuming eddy diffusion coefficients of 10^8 and 10^4 [cm²·s⁻¹], respectively. Hexagrams also illustrate these O/H ratios with [C + N + S] of $100 \times Z_\odot$ but assuming an intrinsic temperature (T_{int}) of 100 K. Crosses represent the K2-18 b scenario with $100 \times Z_\odot$, based on the T–P profile from Wogan et al. (2024). Blue symbols indicate the model simulated by EPACRIS (in this work), and black symbols represent the model by Wogan et al. (2024). The primary differences between the two models lie in the chemical networks and the eddy diffusion coefficient profiles used for modeling. An asterisk indicates $223 \times Z_\odot$. A white square with light blue error bars indicates the JWST observation of K2-18 b (Madhusudhan et al. 2023), and a white square with magenta error bars indicates the JWST observation of TOI-270 d (Benneke et al. 2024). Each color represents the model simulations for the corresponding planets: blue and black for K2-18 b, green for LP 791-18 c, red for TOI-270 d, and magenta for TOI-270 d assuming $A_b = 0$. The colored shaded box regions indicate the implied constraints on the deep interior H_2O-to-H_2 ratios—or envelope O/H ratio—of the corresponding planets based on current studies (light blue for K2-18 b and magenta for TOI-270 d). A much lighter blue shaded box region indicates the constraints when accounting for the hotter intrinsic temperature ($T_{int} = 100$ K) case of K2-18 b with $100 \times Z_\odot$. Gray dotted lines represent standard multipliers of solar metallicity ($1\times$, $10\times$, $100\times$, and $223\times$), aiding in contextualizing the current study against conventional benchmarks in solar metallicity.

observations (Benneke et al. 2024). Since Benneke et al. (2024) also provide a constraint on TOI-270 d's metallicity of approximately $223 \times Z_\odot$ (note that this corresponds to H_2:$H_2O = 80$:20), we ran additional photochemical modeling assuming $A_b = 0.3$ (i.e., $T_{eq} = 354$ K), an intrinsic temperature (i.e., T_{int}) of 60 K, and an eddy diffusion coefficient of

10^6 [$cm^2\,s^{-1}$]. As shown in Figure 1, the resulting CO_2/CH_4 ratio, denoted by a red asterisk, is consistent with the JWST-measured CH_4 and CO_2 and also falls within the deep interior H_2O/H_2 ratio constraint presented in this work. This demonstrates the robustness of the current framework for inferring the deep interior O/H ratio using 1D photochemical modeling, particularly when combined with observational data.

3.1.2. Using Individual Species Abundances as Further Constraints

As described in Section 3.1.1, the upper atmospheric CO_2/CH_4 ratio can be a powerful tool for constraining the bulk envelope H_2O/H_2 ratio. However, this metric does not retain information about the absolute abundances of carbon, nitrogen, and sulfur species in the envelope. It is therefore crucial to investigate whether the abundance of individual gases could provide additional constraints for characterizing the atmosphere and envelope of temperate sub-Neptunes. For instance, could measurements of additional gases help distinguish a T_{int} of 60 K versus 100 K for a planet like K2-18 b? In this section, we explore the behavior of several individual species across various planetary envelope scenarios of temperate sub-Neptunes.

Figure 2 shows the upper atmospheric CO_2, CH_4, CO, NH_3, carbonyl sulfide (OCS), and SO_2 molecular mixing ratios plotted against the deep interior H_2O/H_2 ratios for various planetary envelope scenarios. Generally, a clear pattern emerges between CO_2 and CH_4. These two molecules exhibit opposite behaviors—CO_2 predominates in water-rich envelopes (i.e., deep interior $H_2O/H_2 \geqslant 0.1$), while CH_4 is more abundant in H_2-rich envelopes. Notably, in scenarios with a deep interior $H_2O/H_2 \sim 1$, the presence of both gases is nearly balanced.

Similar to CO_2, CO is favored in an oxidizing environment. However, if there is an excess of oxidizers compared to CO, it will remain fully oxidized as CO. Therefore, it is challenging to exclusively determine whether the atmosphere is H_2-dominated or H_2O-dominated based solely on the CO abundance. Nevertheless, our model indicates that the CO mixing ratio consistently exceeds 1000 ppm if the C abundance is greater than $100 \times Z_\odot$, as shown in Figure 2, identifying CO as a strong indicator of a C-rich planetary envelope. Although the retrieved detection significance of CO abundance is relatively less credible compared to CO_2 and CH_4 due to its sparse infrared absorption line-list density, the largest upper limits of 10^{-3} retrieved from Madhusudhan et al. (2023) suggest that the carbon abundance should be less than $100 \times Z_\odot$. Consequently, the upper atmospheric CO_2 molecular mixing ratio of Wogan et al.'s (2024) modeling that assumes $100 \times Z_\odot$ for K2-18 b (black cross in Figure 2) might not be able to explain the JWST observations of K2-18 b. However, our model, which assumes a carbon abundance of $10 \times Z_\odot$ and a H_2:$H_2O = 50$:50 ratio can still explain all retrieved JWST constraints on CO_2, CH_4, and CO (Madhusudhan et al. 2023). In the case of TOI-270 d, the retrieved upper limit of CO abundance was $10^{-1.46} \sim 0.035$, consistent with all scenarios of our model.

Similar to CH_4, NH_3 indicates reducing envelope conditions (H_2-rich) as shown in Figure 2 and could be a sensitive indicator for constraining the deep interior H_2O/H_2 ratio. For instance, if adopting NH_3's largest upper limits of $10^{-4.46} \sim 0.000035$ retrieved for K2-18 b from Madhusudhan et al. (2023), all scenarios with a nitrogen abundance of $100 \times Z_\odot$ are already ruled out. However, it is important to note that the entire envelope could be intrinsically nitrogen-poor, as N-bearing species can effectively dissolve into the mantle beneath the envelope (Shorttle et al. 2024). This explanation was also proposed for the NH_3 depletion (upper limits of $10^{-4.27}$) observed in TOI-270 d (Benneke et al. 2024).

The upper atmospheric mixing ratios of OCS with respect to the deep interior H_2O-to-H_2 ratios exhibit very interesting features. As shown in Figure 2, regardless of the exact OCS abundance being sensitive to K_{zz} (see blue upward- and downward-pointing triangles), the upper atmospheric OCS mixing ratio is generally predicted to be above $\sim 10^{-5}$ (sufficient to appear as a specific spectral feature at 4.8–4.9 μm, as shown in Figure 5) for deep interiors enriched with more than 10% H_2O across various temperate sub-Neptune scenarios, with T_{eq} ranging from 255 to 387 K. Moses et al. (2013) investigated the compositional diversity of OCS in hot Neptune-sized exoplanets using a thermochemical-equilibrium model in the framework of solar metallicity, but its abundance was less than 1 ppm even at $500 \times Z_\odot$ (see Figure 5 in Moses et al. 2013). However, in our modeling, the OCS formation mechanism is different since we are investigating the case of temperate sub-Neptune exoplanets having an H_2O-rich interior. As described in detail later in Sections 3.2.1 and 3.3.1, the OCS formation was attributed to the enriched water content in the deep interior, resulting in an oxidizing envelope that favors carbon-bearing species in the form of CO and CO_2. Sulfur, primarily from H_2S, then reacts with this CO to form OCS (Scheme 1), which is then transported to the upper atmospheric region observable by the JWST. Additional OCS formation occurs at higher altitudes due to increased sulfur abundance from continuous H_2S photodissociation in the presence of CO (Scheme F1). The OCS formation is thus a result of the oxidative chemistry due to the water-rich envelope. This suggests that OCS is a strong indicator of a water-rich envelope for temperate sub-Neptunes, highlighting OCS as an indicator of temperate sub-Neptune envelopes with over 10% H_2O.

As shown in Figure 2, species such as CO_2, CH_4, NH_3, and OCS exhibit intuitive and consistent behavior with respect to the deep interior O/H ratio. However, the upper atmospheric SO_2 mixing ratio displays a somewhat indirect pattern compared to other species, indicating that its formation pathways are varied. Multiple factors—including T–P structure, absolute sulfur abundance, and O/H ratio—affect SO_2 formation, making it more complex. Nonetheless, SO_2 formation pathways can be divided into two representative regimes, as detailed in Appendix E.

Our models spanning various water-rich envelope scenarios do not always predict SO_2 levels above 10 ppm (which is sufficient to appear as spectral features in JWST observations). However, any SO_2 level above 10 ppm in our model indicates a deep interior with more than 10% H_2O inside. For this reason, along with OCS, our model suggests that any future detection of SO_2 in temperate sub-Neptune atmospheres indicates a water-rich interior of at least more than 10% H_2O.

Although we only used CO_2+CH_4 in the current study due to the limited or absent observational constraints on N- or S-bearing species, other species such as NH_3, OCS, or SO_2 could serve as additional tools to more precisely constrain the deep interior H_2O/H_2 ratio along with the absolute N or S abundance as described in this section.

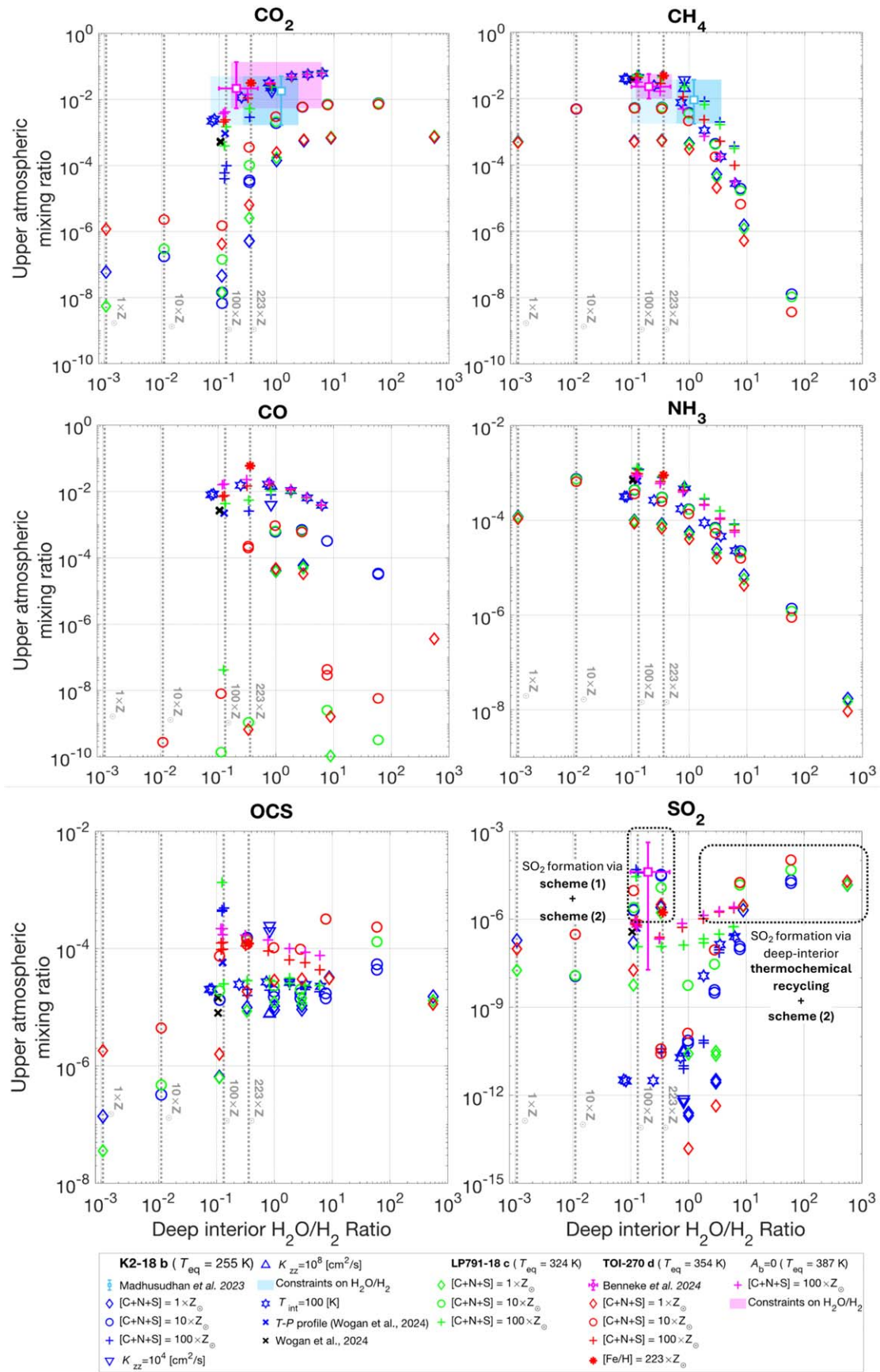**Figure 2.** The upper atmospheric ($P = 0.1$–2 mbar) CO_2, CH_4, CO, NH_3, OCS, and SO_2 molecular mixing ratios plotted against the deep interior ($P = 200$ bars) H_2O-to-H_2 ratios, respectively. All notations follow Figure 1. The black dotted boxes indicate the major formation pathways that contribute to SO_2 formation.
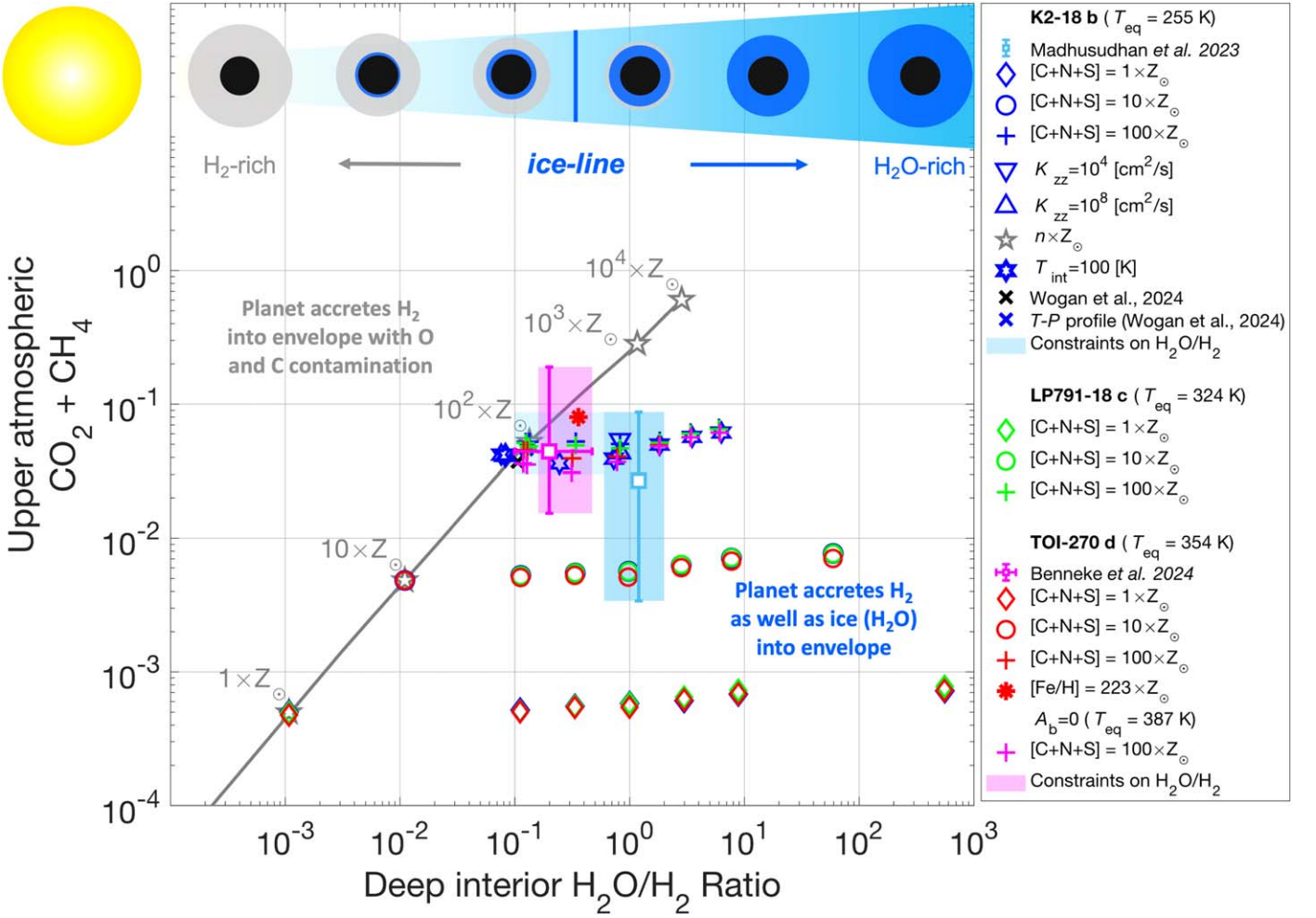
Figure 3. The figure shows a schematic diagram of the feeding zone of planets in the protoplanetary disk with respect to the ice line on the top and the upper atmospheric ($P = 0.1$–2 mbar) CO_2 + CH_4 mixing ratios plotted against the deep interior ($P = 200$ bars) H_2O-to-H_2 ratios on the bottom. It should be noted that the position of the ice line is depicted arbitrarily to better illustrate the concept of the current study. All notations follow Figure 1. The only difference is that the constraints on the H_2O/H_2 ratio for each planet are now based on the combination of the CO_2/CH_4 ratio (Section 3.1.1) and individual abundances (Section 3.1.2).

3.1.3. Constraining the Building Blocks of Temperate Sub-Neptunes

Figure 3 presents a comprehensive plot after integrating all the constraints from the CO_2/CH_4 ratio and each of the mixing ratios of CO_2 and CH_4, as described in Sections 3.1.1 and 3.1.2. Notably, in Figure 3, we can constrain the carbon abundance included in the planetary envelope to within the range of $10-100 \times Z_\odot$ for K2-18 b and approximately $40-500 \times Z_\odot$ for TOI-270 d using absolute CO_2 and CH_4 mixing ratios. Particularly, the carbon abundance for K2-18 b constrained within the range of $10-100 \times Z_\odot$ aligns well with the carbon abundance implied from the CO abundance shown in Section 3.1.2 and Figure 2.

According to Figure 3, the most probable scenario for TOI-270 d is close to H_2:H_2O = 75:25 and [C + N + S] = $100 \times Z_\odot$ assuming either $A_b = 0$ (magenta plus signs) or 0.3 (red plus signs). Although the uncertainty is substantial, the SO_2 mixing ratio constrained from the JWST observation of TOI-270 d by Benneke et al. (2024) also falls within this O/H ratio range as shown in the SO_2 panel of Section 3.1.2. In the case of K2-18 b, two scenarios—H_2:H_2O = 50:50 and H_2:H_2O = 25:75, both with [C + N + S] = $100 \times Z_\odot$ scenarios (represented by blue plus signs)—fall within the constraints from the chemical mapping (i.e., thick blue shaded area).

Furthermore, Figure 3 reveals some new insights: TOI-270 d can still fit within the conventional solar metallicity framework, depicted by a gray solid line (particularly simulated for various K2-18 b planetary envelope scenarios) in Figure 3. If we maintain this framework, TOI-270 d would require a metallicity significantly above the $100 \times Z_\odot$ value. This is corroborated by a red asterisk on the plot, representing the retrieved constraint on the metallicity of $\sim223 \times Z_\odot$ from the JWST observation by Benneke et al. (2024). However, K2-18 b cannot be explained within this conventional solar metallicity framework (note: a C/O ratio of 0.134–0.138 is required to explain the JWST observations of K2-18 b shown in Figure 3). Instead, its characteristics (i.e., thicker blue shaded region) suggest efficient ice accretion within the protoplanetary disk, implying that planetary formation occurred close to or beyond the ice line (Burn et al. 2024). This underscores the importance of the O/H ratio as a pivotal variable in classifying exoplanets, potentially revealing their original locations of planetary formation. By combining this chemical mapping method with many upcoming observational data, we can determine whether the planet accretes H_2 into the envelope with other elements or efficiently accretes H_2O in the form of ice into its envelope, as shown in Figure 3.
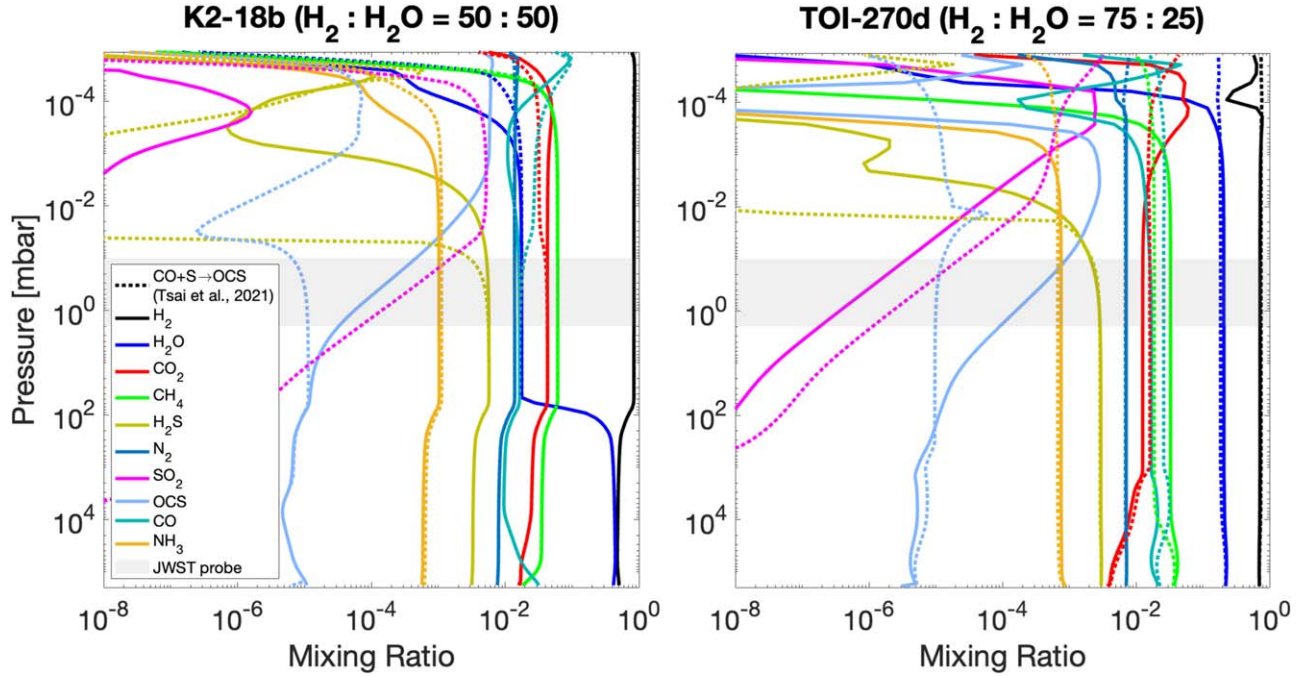
Figure 4. Vertical molecular mixing ratio profiles of major species for the constrained scenarios for K2-18 b and TOI-270 d in Section 3.1: K2-18 b with a H_2:H_2O ratio of 50:50 and [C + N + S] of $100 \times Z_\odot$ assuming $A_b = 0.3$ (left) and TOI-270 d with a H_2:H_2O ratio of 75:25 and [C + N + S] of $100 \times Z_\odot$ assuming $A_b = 0$ (right). Each color indicates the corresponding species: H_2 in black, H_2O in blue, CO_2 in red, CH_4 in green, H_2S in dark yellow, N_2 in dark blue, SO_2 in magenta, OCS in light blue, CO in teal, and NH_3 in light brown. The dotted lines indicate major species' vertical mixing ratio profiles when using the rate coefficient of Scheme 2 adopted from Tsai et al. (2021). The gray shaded area indicates the JWST primary probing range (i.e., $P = 0.1–2$ mbar; Rustamkulov et al. 2023).

3.2. The Atmosphere of K2-18 b

3.2.1. Overall Chemistry in the Atmosphere of K2-18 b

The left panel of Figure 4 shows the simulated vertical molecular mixing ratio profiles of major species for the scenario close to the most probable scenario for K2-18 b (i.e., H_2:H_2O = 50:50 with [C + N + S] = $100 \times Z_\odot$) according to the chemical mapping detailed in Section 3.1. The first notable thing to look at is the condensation behavior of water at $P \sim 10^2$ mbar. This is consistent with the computed T–P profiles for various scenarios of K2-18 b as shown in Figure B1 in Appendix B. As illustrated in Figure B1, water condensation would begin around $P \sim 10^2$ mbar, where the condensation curves for H_2O (Buck 1981) intersect with the T–P profiles for various O/H ratios with [C + N + S] = $100 \times Z_\odot$ scenarios for K2-18 b (see blue solid lines in Figure B1). Consequently, the JWST-observable region of the upper atmosphere will have a H_2-dominated atmosphere with less than ~1% of H_2O, enhancing spectral features due to a decreased mean molecular weight (Miller-Ricci et al. 2008). The mixing ratios of other molecular species such as H_2, CH_4, CO_2, N_2, H_2S, and NH_3 in the JWST probe region are primarily determined by the deep interior thermal chemistry and are quenched at pressures greater than 10^4 mbar before being transported upward. This quenching behavior is expected since the equilibrium temperatures of temperate sub-Neptunes are low, leading to longer chemical lifetimes relative to the vertical mixing timescale. At higher altitudes (i.e., pressures lower than 0.1 mbar), UV-driven photochemistry dominates, photodissociating species including H_2O, CO_2, H_2S, and NH_3.

Another notable feature is the significant presence of OCS in the JWST-observable region, as shown in the left panel of Figure 4. OCS primarily forms in the deep interior through the reaction between sulfur from H_2S and CO, which is the

favorable carbon-bearing species in H_2O-rich oxidizing envelopes:

$$H_2S \rightarrow H_2 + S$$
$$S + CO \xrightarrow{M} OCS, \qquad (1)$$

with M representing any third-body molecule. Further details of sulfur chemistry in the atmosphere of K2-18 b can be found in Appendix F. It is noteworthy that the rate coefficient of the termolecular reaction,

$$S + CO \xrightarrow{M} OCS, \qquad (2)$$

has significant uncertainty, as previously discussed in Ranjan et al. (2020) and Tsai et al. (2021). Potentially, this uncertainty can lead to a significant difference in the composition of dominant sulfur-bearing species (e.g., OCS as dominant or SO_2 as dominant) in the upper atmosphere, where temperatures are usually very low, below 500 K. This is because even a small uncertainty in the activation energy in the exponential term of the Arrhenius rate equation can lead to substantial deviations from the actual reaction rate at these lower temperatures. Additionally, unlike fuel chemistry involving CHO species (or maybe including N), we lack extensive details on sulfur chemistry (e.g., sulfur chemistry induced by excited S(^{1}D), which would be important in the upper atmosphere but poorly understood). For this reason, we need a systematic approach to address this issue in future studies.

In the current study, RMG adopts the OCS thermal dissociation rate coefficient measured by the shock tube experiments conducted by Oya et al. (1994) and Woiki & Roth (1995). The rate coefficient for the reverse direction (i.e., Scheme 2) was then calculated using the Gibbs free energies of
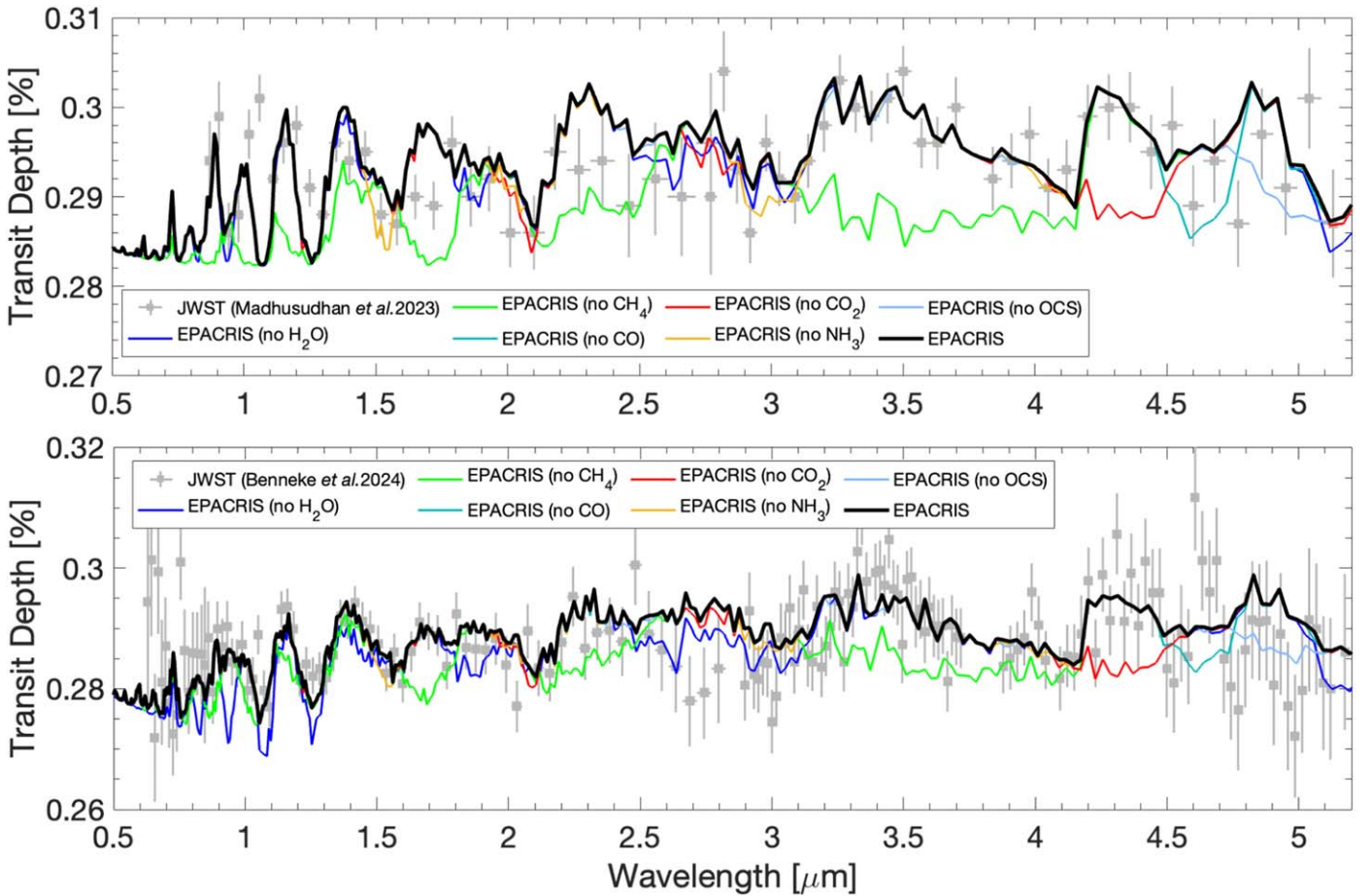
Figure 5. Comparisons between the theoretical transmission spectra generated by EPACRIS (solid lines) and the JWST observations for (top) the $H_2:H_2O = 50:50$ and $[C + N + S] = 100\times$ solar metallicity scenario of K2-18 b assuming $A_b = 0.3$ corresponding to the solid lines in the left panel of Figure 4 and (bottom) the H_2: $H_2O = 75:25$ and $[C + N + S] = 100\times$ solar metallicity scenario of TOI-270 d assuming $A_b = 0$ corresponding to the solid lines in the right panel of Figure 4. The gray symbols with error bars indicate JWST observations of the corresponding exoplanets taken from Madhusudhan et al. (2023) for K2-18 b (top) and Benneke et al. (2024) for TOI-270 d (bottom). Each color represents a spectrum generated by excluding specific species: green for no CH_4, red for no CO_2, light blue for no OCS, blue for no H_2O, teal for no CO, light brown for no NH_3, and black for all species included.

the corresponding species, which is the same rate coefficient adopted for reaction 2 in Zahnle et al. (2016). The sensitivity of the vertical mixing ratio profiles of both K2-18 b's and TOI-270 d's most probable scenarios to the OCS recombination rate is shown in Figure 4, with the corresponding synthesized transmission spectra available in Appendix F. As illustrated in Figure 4, although most major species show no significant changes in their predicted vertical mixing ratios, the dominant sulfur-bearing species now shifts from OCS (solid lines, which adopt the rate coefficient of Scheme 2 adopted from Zahnle et al. 2016) to SO_2 (dotted lines, which adopt the rate coefficient of Scheme 2 estimated from Tsai et al. 2021). Although the statement connecting any potential detection of SO_2 or OCS in temperate sub-Neptune atmospheres to a water-enriched interior remains unchanged, this strongly suggests the need for future studies to accurately estimate the rate coefficient for Scheme 2 through either quantum chemical calculations or experimental reaction kinetic measurements.

3.2.2. Theoretical Transmission Spectra of the Atmosphere of K2-18 b Generated by EPACRIS

The top panel of Figure 5 compares EPACRIS-generated theoretical transmission spectra with JWST observations of K2-

18 b (Madhusudhan et al. 2023). The EPACRIS prediction aligns well with the JWST data, particularly in capturing the CO_2 (red) and CH_4 (green) features identified by Madhusudhan et al. (2023). Although NH_3 was not detected in the retrieval by Madhusudhan et al. (2023), EPACRIS-generated transmission spectra suggest its presence at around $3\,\mu m$, as well as CO around $4.6\,\mu m$ and, notably, OCS around $4.8\,\mu m$. This highlights the need for more detailed observations at these spectral windows to detect these molecules, which may have been overlooked due to low resolution or insufficient transits. Any potential detection of NH_3 would be particularly significant as it can rule out the possibility of the Hycean scenario for K2-18 b (Hu et al. 2021; Madhusudhan et al. 2021; Tsai et al. 2021; Yu et al. 2021), underscoring the importance of detailed observations. Additionally, the detection of OCS would be noteworthy since this molecule has not been detected in exoplanetary atmospheres so far.

3.3. The Atmosphere of TOI-270 d

3.3.1. Overall Chemistry in the Atmosphere of TOI-270 d

The right panel of Figure 4 shows the simulated vertical molecular mixing ratio profiles of major species for the

scenario close to the most probable scenario for TOI-270 d (i.e., H_2:$H_2O = 75$:25 with $[C + N + S] = 100 \times Z_\odot$ assuming $A_b = 0$) according to the chemical mapping detailed in Section 3.1. Different from the K2-18 b scenario, no significant condensation of water is observed due to the much higher equilibrium temperature of TOI-270 d ($T_{eq} = 387$ K) compared to that of K2-18 b ($T_{eq} = 255$ K). As illustrated in Figure B1, all T–P profiles of various planetary envelope composition scenarios of TOI-270 d (see red and magenta lines in Figure B1) lie above the water condensation line (Buck 1981). Consequently, the entire atmosphere contains a significant amount of water ($\geqslant 10\%$), leading to decreased spectral features due to an increased mean molecular weight from H_2O. The overall chemistry regarding molecular species such as H_2, CH_4, CO_2, N_2, H_2S, NH_3, and OCS is similar to that of K2-18 b, as described in Section 3.2.1. In contrast, the upper atmosphere of TOI-270 d is richer in H_2O compared to K2-18 b's upper atmosphere, where water condensation occurs. This leads to increased SO_2 formation due to more H_2O being photolyzed by UV radiation, forming H and OH radicals that gradually oxidize reduced sulfur species (e.g., H_2S, S, and S_2) into SO_2 (Tsai et al. 2023).

3.3.2. Theoretical Transmission Spectra of the Atmosphere of TOI-270 d Generated by EPACRIS

The bottom panel of Figure 5 compares EPACRIS-generated theoretical transmission spectra with JWST observations of TOI-270 d (Benneke et al. 2024). The EPACRIS prediction generally aligns well with the JWST data, particularly in capturing the CO_2 (red) and CH_4 (green) features identified by Benneke et al. (2024). Unlike K2-18 b, water is present in the JWST-observable part of TOI-270 d's atmosphere and contributes to the spectral features. Although a strong spectral feature around 4.7 μm cannot be solely explained by CO-attributed absorption, EPACRIS-generated transmission spectra suggest that the spectral modulation around 4.8 μm is due to OCS. This, again, underscores the importance of detailed observations at this spectral range.

3.4. Discussions

In this study, we propose measuring the abundances of CO_2 and CH_4 (readily observable within 3–5 μm by JWST) as the primary metric to determine the bulk envelope H_2O-to-H_2 ratio of temperate sub-Neptunes. Additionally, we suggest that other species such as CO, NH_3, OCS, and SO_2 (see Section 3.1.2) could provide further constraints on the envelope composition despite uncertainties in the deep interior temperature. Notably, the inference of the envelope H_2O-to-H_2 ratio does not involve direct measurements of H_2O in the observable part of the atmosphere, which can be depleted due to condensation.

Breaking the degeneracy in scenarios involving a hot interior is an intriguing question. In the recent study of warm Neptune WASP-107 b ($T_{eq} = 750$ K), the combination of CO_2 and CH_4, which are jointly sensitive to T_{int}, was used to decipher the intrinsic temperature of a warm-Neptune exoplanet ($T_{int} \geqslant 400$ K; Sing et al. 2024; Welbanks et al. 2024). As mentioned in Section 3.1.1, the model results are sensitive to T_{int} when the atmosphere is relatively H_2-dominated ($\leqslant 25\%$ water-rich), as shown in Figures 1 and 2. Within the range of $T_{int} \leqslant 100$ K, this sensitivity largely vanishes when the envelope is highly enriched in H_2O. It would be an interesting future study to determine if this insensitivity to T_{int} in H_2O-enriched cases still applies when $T_{int} \geqslant 400$ K (e.g., WASP-107 b; Sing et al. 2024; Welbanks et al. 2024). Beyond the CO_2–CH_4 abundances and ratio, our model suggests that the detection of SO_2 in a relatively H_2-dominated atmosphere ($\leqslant 20\%$ internal H_2O envelope) of temperate sub-Neptunes could disfavor a high intrinsic temperature ($T_{int} \geqslant 100$ K) scenario.

We have identified various novel formation pathways for SO_2 in sub-Neptune atmospheres. Unlike hot or warm Jupiters or Neptunes, temperate sub-Neptunes around M dwarf stars experience lower radiation on their planetary atmospheres, making the photochemical formation mechanism of SO_2 proposed for the atmosphere of WASP-39 b ineffective (Tsai et al. 2023). As shown in Section 3.1.2, SO_2 formation in temperate sub-Neptune atmospheres is complex due to many contributing factors, with a novel mechanism using CO_2 as the oxidizer in weakly H_2O-rich atmospheres and direct thermo-chemical formation in highly H_2O-rich atmospheres. These mechanisms indicate that it is likely to detect SO_2 on exoplanets with a wide range of envelope composition and temperatures, and the interpretation of each detection will likely require detailed photochemical modeling.

As shown in Figure B1, the equilibrium temperature differences between K2-18 b and TOI-270 d distinctly categorize these planets based on whether water condensation occurs (K2-18 b) or not (TOI-270 d). The equilibrium temperature of LP 791-18 c falls between these two different regimes, presenting possible degenerate scenarios. Therefore, by performing chemical mapping of such temperate sub-Neptunes (e.g., LP 791-18 c), we can cover a broad range of temperate sub-Neptunes with equilibrium temperatures (T_{eq}) between 250 and 400 K (corresponding to 221 confirmed sub-Neptunes according to NASA's Exoplanet Archive 2024). With the upcoming JWST observations of LP 791-18 c and many other future observations of temperate sub-Neptunes, the current chemical mapping will significantly enhance our understanding of a planet's interior O/H composition and potentially its planetary formation mechanisms as well.

4. Conclusions

In this study, using self-consistent radiative transfer modeling (M. Scheucher & R. Hu 2024, in preparation) and a rate-based automatic chemical network generator combined with 1D photochemical kinetic-transport atmospheric modeling (Yang & Hu 2024), we have extensively investigated various atmospheric scenarios of temperate sub-Neptunes with equilibrium temperatures (T_{eq}) ranging from 250 to 400 K. We introduce a new framework that utilizes the atmospheric CO_2/CH_4 ratio to gauge the bulk envelope H_2O/H_2 ratio of temperate sub-Neptunes, providing new insights into their formation locations relative to the ice line. Furthermore, our models suggest that any potential detection of OCS and SO_2 serves as a strong indicator of at least a 10% water-rich envelope in temperate sub-Neptunes.

Benchmarking with recent JWST observations of two well-known temperate sub-Neptunes, K2-18 b (Madhusudhan et al. 2023) and TOI-270 d (Benneke et al. 2024), our modeling results suggest the following. The most probable scenario for TOI-270 d's envelope is H_2:$H_2O \sim 75$:25 with $[C + N + S] = 100 \times Z_\odot$, implying an original location inside the ice line during planetary formation. For K2-18 b's envelope, the ratio is H_2:$H_2O \sim 50$:50 with $[C + N + S] \leqslant 100 \times Z_\odot$, implying a

location beyond the ice line during planetary formation. The synthesized transmission spectra based on these models showed good agreement with the JWST observations (Madhusudhan et al. 2023; Benneke et al. 2024). Furthermore, our synthesized transmission spectra suggest the potential detection of OCS at approximately 4.8–4.9 μm in both JWST observations of K2-18 b and TOI-270 d. This indicates that these planets might contain at least a 10% H_2O-rich envelope.

While TOI-270 d can be explained by conventional multipliers of solar metallicity, yielding approximately $230 \times Z_\odot$, K2-18 b cannot be solely explained by the conventional solar metallicity framework. This requires considering an additional variable: the deep interior H_2O/H_2 ratio, or planetary O/H ratio, which can potentially reveal the planets' original locations during their formation.

Appendix A
Elemental Parameterization of Planetary Envelopes
(Section 2.1)

This appendix demonstrates a detailed description of the O/H variation mentioned in Section 2.1. Figure A1 and Table A1 present the various planetary envelope composition scenarios for sub-Neptunes as discussed in Section 2.1. We began the O/H variation using the following equation:

$$[H + He + O]_{n \times Z_\odot} = a$$
$$\frac{[H_2O]}{[H_2] + [H_2O]} = x_{acc},$$

where $[H_2O]$ and $[H_2]$ represent water and hydrogen abundance in the envelope, respectively. Therefore, x_{acc} represents the accretion ratio for H_2O. If planetary formation takes place inside the ice line and closer to its parent star, x_{acc} will approach 0 (i.e., H_2-rich). Conversely, if planetary formation occurs beyond the ice line and farther from its parent star, x_{acc} will approach 1 (i.e., H_2O-rich). Consequently, each elemental abundance [H], [O], and [He] will be as in the following equation:

$$[H] = 2([H_2] + [H_2O])$$
$$[He] = \frac{[H]}{11.91} = \frac{2([H_2] + [H_2O])}{11.91}$$
$$[O] = [H_2O] = x_{acc}([H_2] + [H_2O]),$$

where the H/He ratio was maintained at 11.91 to determine the helium abundance (Lodders 2020). Finally, the absolute

elemental abundance for the x_{acc} scenarios would be

$$[H]_{x_{acc}} = a \times \frac{[H]}{[H] + [He] + [O]}$$
$$= \frac{2a}{2 + x_{acc} + \frac{2}{11.91}}$$
$$[He]_{x_{acc}} = a \times \frac{[He]}{[H] + [He] + [O]}$$
$$= \frac{2a}{\left(2 + x_{acc} + \frac{2}{11.91}\right) \times 11.91}$$
$$[O]_{x_{acc}} = a \times \frac{[O]}{[H] + [He] + [O]}$$
$$= \frac{a x_{acc}}{2 + x_{acc} + \frac{2}{11.91}} \quad (A1)$$

$$[H + He + O]_{x_{acc}} = [H + He + O]_{n \times Z_\odot} = a.$$

Overall, the mixing ratio of [H + He + O] is unchanged, thus retaining the original ratios of carbon, nitrogen, and sulfur fixed.

As an example, for the $H_2:H_2O = 90:10$ accretion scenario at $1 \times Z_\odot$ (the second row and fourth column in Table A1),

$$a = 0.921775 + 0.077379 + 0.00495 = 1.004104$$
$$x_{acc} = 0.1.$$

This results in a total H-to-O ratio of 20.00 (which can be approximated using $90 \times 2 + 10 \times 2$ versus 10). Following the same procedure, we progressed through 75:25, 50:50, 25:75, and 10:90, culminating in a completely water-rich envelope at a 0:100 ratio. It should be noted that in the case of $100 \times Z_\odot$, if we assume all oxygen to be in the form of water, then the amount of water already exceeds the abundance of water in the $H_2:H_2O = 90:10$ scenario. Consequently, the oxygen abundance at $100 \times Z_\odot$ (i.e., $H_2:H_2O = 100:0$) is slightly higher than the oxygen abundance at $H_2:H_2O = 90:10$, as seen by comparing the third and fourth columns in the 20th row in Table A1.

We applied these 21 scenarios (three different solar metallicity cases × seven different O/H ratios or H_2-to-H_2O accretion ratios) across three temperate sub-Neptunes, K2-18 b, LP 791-18 c, and TOI-270 d, resulting in a total of 63 scenarios. We investigated 17 additional scenarios to understand model sensitivities. For K2-18 b, we tested the sensitivity of the $H_2:H_2O = 50:50$ and $[C + N + S] = 100 \times Z_\odot$ scenario to the eddy diffusion coefficients (K_{zz}) with values of 10^4 and 10^8 cm^2 s^{-1}, compared to the standard 10^6 cm^2 s^{-1} mainly adopted in this study. We also explored seven different O/H scenarios, maintaining $[C + N + S]$ at $100 \times Z_\odot$, using a T–P profile computed for $100 \times Z_\odot$ and an intrinsic temperature (T_{int}) of 100 K to test the sensitivity of the model to a higher T_{int} of 100 K compared to the standard 60 K mainly adopted in this study. For TOI-270 d, we evaluated one scenario assuming $223\times$ solar metallicity to benchmark against the metallicity constraint retrieved from Benneke et al. (2024). Additionally, we investigated seven different O/H scenarios, maintaining $[C + N + S]$ at $100\times$ solar metallicity, assuming a Bond albedo of 0. Overall, we analyzed 74 ($63 + 2 + 1 + 1 + 7$) planetary atmospheric structures (T–P profiles) and 80 ($63 + 2 + 7 + 1 + 7$) planetary atmospheric photochemical models.
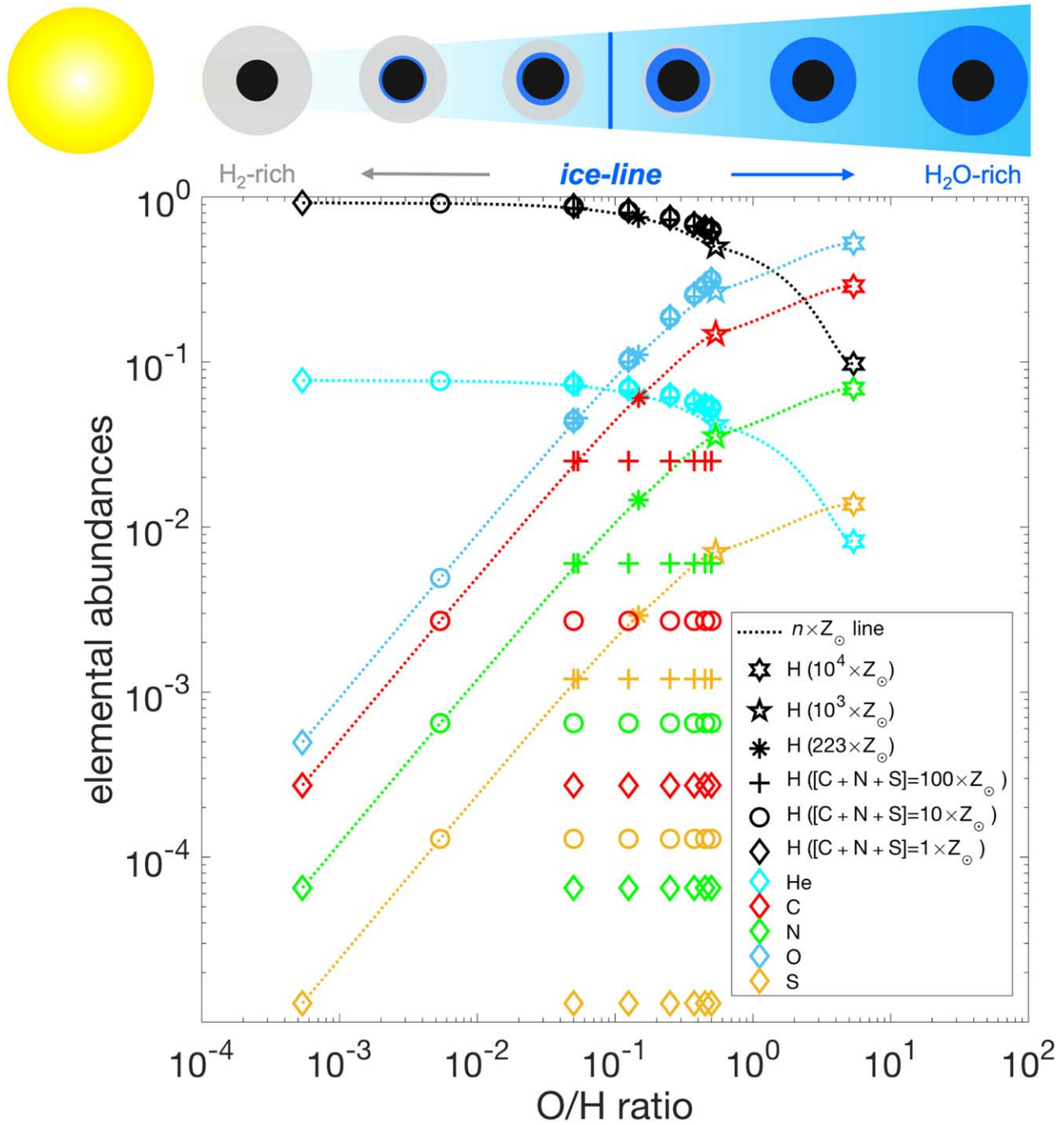
Figure A1. (Top) A schematic diagram of the protoplanetary disk with respect to the ice line (note that the position of the ice line is depicted arbitrarily to better illustrate the concept of the current study). (Bottom) Elemental abundances in various planetary envelope composition scenarios plotted against the oxygen-to-hydrogen (O/H) ratio, spanning from hydrogen-rich (i.e., lower O/H) to water-rich (i.e., higher O/H) envelopes. The O/H ratio along the X-axis represents the location within the protoplanetary disk relative to the ice line, where planets with H_2-rich envelopes typically form inside the ice line and those with H_2O-rich envelopes form beyond the ice line, as depicted in the top figure. Each open symbol corresponds to different elemental abundance scenarios ($Z_\odot$ represents solar metallicity): hexagrams for $10^4 \times Z_\odot$; asterisks for $10^3 \times Z_\odot$ solar metallicity; plus signs for carbon, nitrogen, and sulfur abundances, [C + N + S], of $100 \times Z_\odot$; circles for [C + N + S] = $10 \times Z_\odot$; and diamonds for [C + N + S] = $1 \times Z_\odot$. Colors represent different elemental species: hydrogen (black), helium (cyan), carbon (red), nitrogen (green), oxygen (light blue), and sulfur (light brown). Dotted lines indicate standard multipliers of solar metallicity for each element.

Table A1
Elemental Composition Profiles Utilized to Investigate a Range of Planetary Atmospheric Scenarios in This Study

H_2:H_2O Accretion Ratio		H$_2$-rich		$\Longleftrightarrow$ 75:25	H$_2$O-rich			
		100:0	90:10		50:50	25:75	10:90	0:100
1×	H	0.921775	0.881567	0.826877	0.749393	0.685186	0.651685	0.631113
	He	0.077379	0.074004	0.069413	0.062909	0.057519	0.054706	0.052979
	C	0.000272	0.000272	0.000272	0.000272	0.000272	0.000272	0.000272
	N	0.000065	0.000065	0.000065	0.000065	0.000065	0.000065	0.000065
	O	0.000495	0.044078	0.103360	0.187348	0.256945	0.293258	0.315557
	S	0.000013	0.000013	0.000013	0.000013	0.000013	0.000013	0.000013
10×	H	0.914815	0.878810	0.824291	0.747049	0.683043	0.649647	0.629140
	He	0.076795	0.073773	0.069196	0.062712	0.057339	0.054535	0.052814
	C	0.002700	0.002700	0.002700	0.002700	0.002700	0.002700	0.002700
	N	0.000648	0.000648	0.000648	0.000648	0.000648	0.000648	0.000648
	O	0.004913	0.043941	0.103036	0.186762	0.256141	0.292341	0.314570
	S	0.000129	0.000129	0.000129	0.000129	0.000129	0.000129	0.000129
100×	H	0.850591	0.853369	0.800428	0.725422	0.663269	0.630840	0.610926
	He	0.071404	0.071637	0.067193	0.060896	0.055679	0.052956	0.051285
	C	0.025103	0.025103	0.025103	0.025103	0.025103	0.025103	0.025103
	N	0.006022	0.006022	0.006022	0.006022	0.006022	0.006022	0.006022
	O	0.045679	0.042668	0.100053	0.181356	0.248726	0.283878	0.305463
	S	0.001201	0.001201	0.001201	0.001201	0.001201	0.001201	0.001201
223×	H	0.748399						
	He	0.062838						
	C	0.060745						
	N	0.014572						
	O	0.110539						
	S	0.002907						
1000×	H	0.499741						
	He	0.041960						
	C	0.147484						
	N	0.035379						
	O	0.268377						
	S	0.007059						
10,000×	H	0.097516						
	He	0.008188						
	C	0.287791						
	N	0.069036						
	O	0.523694						
	S	0.013775						

Note. We explored atmospheres spanning from hydrogen-rich (H$_2$) to water-rich (H$_2$O) compositions and varying from 1× to 100× solar metallicity. For each scenario, we systematically varied the H$_2$-to-H$_2$O ratio, beginning at 100:0 and progressing through intermediate stages of 90:10, 75:25, 50:50, 25:75, and 10:90, until reaching a completely water-rich environment at a 0:100 ratio. This range of scenarios, detailed in the main text and depicted in Figure A1, illustrates variations in planetary formation locations relative to the ice line. Additionally, some cases were modeled at higher metallicities, including 223×, 1000×, and 10,000× solar metallicity.

Appendix B
The T–P Profiles for Various Planetary Envelope Scenarios (Section 2.2)

This appendix provides detailed information on the radiative transfer modeling using EPACRIS-Climate (M. Scheucher & R. Hu 2024, in preparation) as described in Section 2.2. Figure B1 represents the resulting T–P profiles calculated for different planetary envelope scenarios.

EPACRIS-Climate (M. Scheucher & R. Hu 2024, in preparation) uses the two-stream method (Heng & Marley 2018) to compute radiative fluxes and incorporates both dry and moist adiabatic adjustments, following the methodology of Graham et al. (2021). In brief, the climate module of EPACRIS automatically applies moist adiabats when condensation occurs and dry adiabats when condensation does not occur. Water is considered a condensable component, and its atmospheric concentration is self-consistently adjusted in line with the moist adiabats. Some might argue that in an H$_2$ background, moist convection is inhibited once water surpasses a critical moisture threshold, resulting in a steep lapse rate (Leconte et al. 2017, 2024; Innes et al. 2023). Also, in the environment of the interior where $T \geqslant \sim 650\,\mathrm{K}$ $P \geqslant \sim 200$ bars, water becomes supercritical and is expected to be miscible with other gases (Pierrehumbert 2023; Benneke et al. 2024). Although the current study does not model the deep interior beyond 200 bars, the climate module of EPACRIS currently does not account for supercritical fluid adiabats. Therefore, addressing these features could be a potential future development in the climate module of EPACRIS. Presently, EPACRIS considers the impact of a hotter
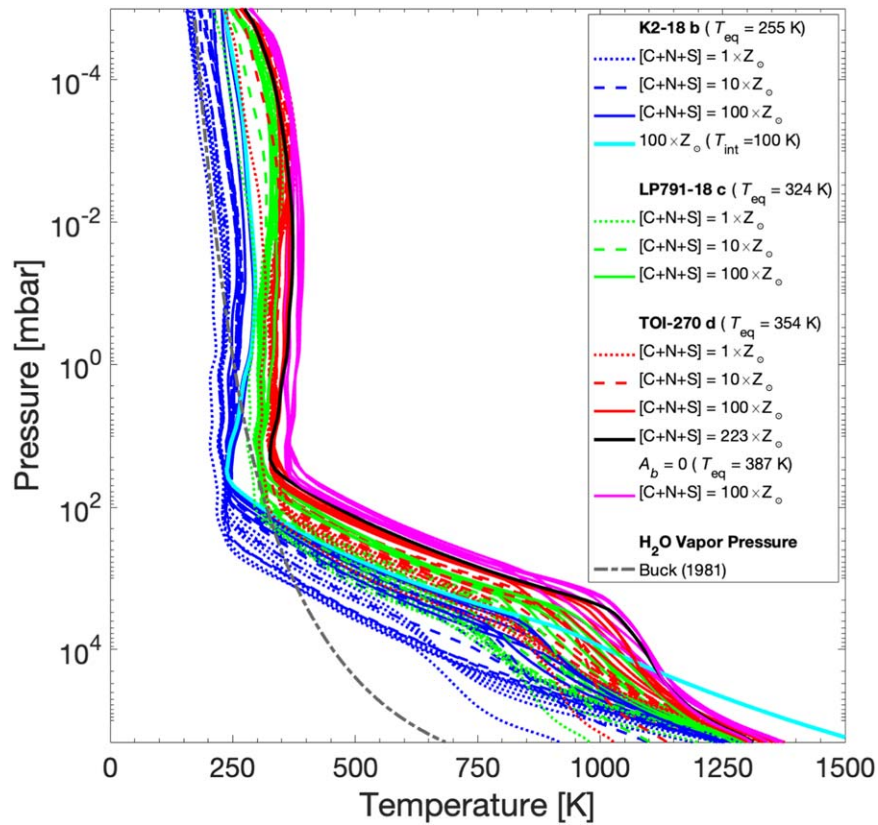
Figure B1. The figure shows 72 T–P profiles for different planetary envelope scenarios, calculated as described in Section 2.2 (1000× and 10,000× solar metallicity cases for K2-18 b are omitted for simplicity). $Z_\odot$ represents solar metallicity. Unless otherwise specified, the planetary equilibrium temperature (i.e., T_{eq}) assumes an A_b of 0.3 and an intrinsic temperature (T_{int}) of 60 K by default. Each color corresponds to a specific planetary envelope scenario: blue for K2-18 b, cyan for K2-18 b assuming T_{int} = 100 K, green for LP 791-18 c, red for TOI-270 d, black for the 223 × $Z_\odot$ scenario of TOI-270 d, and magenta for TOI-270 d assuming A_b = 0. The solid lines (except cyan and black) represent seven different O/H scenarios (i.e., H_2:H_2O from 100:0 to 0:100) with the elemental composition of carbon, nitrogen, and sulfur ([C + N + S]) of 100 × $Z_\odot$, dashed lines for 10 × $Z_\odot$, and dotted lines for 1 × $Z_\odot$, as detailed in Section 2.1. The gray dotted–dashed line indicates the condensation curves for H_2O (solid and liquid states) from Buck (1981). As illustrated in the figure, only for cases of K2-18 b (i.e., blue and cyan lines), water condenses to form clouds below the photosphere (i.e., the pressure range at ∼1 mbar where the JWST conducts its observations). In contrast, other planets, LP 791-18 c (green lines) and TOI-270 d (red, black, and magenta lines), are too hot for water condensation to occur.

interior on chemical composition, incorporating a higher internal heat flux.

We assumed an intrinsic temperature (T_{int}) of 60 K (Hu 2021). For some cases of K2-18 b scenarios, we tested a larger T_{int} of 100 K to test the sensitivity of the model, since T_{int} can impact deep atmospheric quenching and its result in the upper atmospheric abundances of chemical species (Fortney et al. 2020; Tsai et al. 2021).

By default, we set the planetary Bond albedo (A_b) to an Earth-like value of 0.3 for all planets, including K2-18 b, LP 791-18 c, and TOI-270 d. For TOI-270 d, we additionally explored seven different O/H ratio scenarios while maintaining [C + N + S] = 100 × $Z_\odot$ but with A_b = 0. In all cases, we assumed an average solar zenith angle of 48.19@ (Cronin 2014). The stellar irradiation parameters (S_p in W·m^{-2}) were adopted to be 1368 W·m^{-2} for K2-18 b (Benneke et al. 2019), 3607 W·m^{-2} for LP 791-18 c (Peterson et al. 2023), and 4333 W·m^{-2} for TOI-270 d (Günther et al. 2019).

Appendix C
RMG-generated Species that Are Not Included in the Original EPACRIS Species Library (Section 2.3)

This appendix provides additional information on the chemical reaction network generation using RMG (Gao et al.

2016) as described in Section 2.3 and details the 36 newly included molecular species in the chemical network tailored for H_2O-dominated atmospheres.

In this work, we sampled temperatures ranging from 300 to 1100 K and pressures from 10^{-3} to 10^2 bars to generate chemical networks tailored for a H_2O-rich scenario of temperate sub-Neptunes, as established by previous radiative transfer modeling of K2-18 b (Scheucher et al. 2020).

For initial molecular mixing ratio inputs required for using RMG to generate a reaction network for the targeted system, we used the following: 10^0 for H_2O to account for a H_2O-rich scenario. Additional constraints were based on the recent JWST observations of K2-18 b by Madhusudhan (2023): $10^{-1.89}$ for CH_4 and $10^{-2.05}$ for CO_2, both determined from two-offset retrieved molecular abundances with detection significances of 5σ and 3.2σ, respectively, and $10^{-4.46}$ for S and N, derived from no-offset retrieved molecular abundances with a 2.4σ detection significance for $(CH_3)2S$ and based on the upper limit for nitrogen. These values were later normalized to sum to 1.

The choice of reaction libraries can be found in the supplementary RMG input file. The details of these libraries can be found in the RMG database (RMG 2023). The completed network comprised 92 species and 1950 reactions, detailed in the supplementary CHEMKIN file. Of these, 92 species and 1666 reactions were incorporated into the 1D

Table C1
36 Newly Included Molecular Species in the Chemical Network Tailored for H_2O-dominated Atmospheres by RMG

Species	SMILES[a]	Species	SMILES[a]
CH_2OH[b,c]	[CH]O	HCOH	[C−]=[OH+]
CH_2CHO	[CH2]C=O	H_2CC	[C]=C
CH_2CHOH	C=CO	CH_2CH_2OH	[CH]CO
CHCHO	[CH]=C[O]	HCCOH	C#CO
CHCHOH	[CH]=CO	CH_3CH_2OH	CCO
CH_3CHOH	C[CH]O	OCHCO	O=[C]C=O
$HOCH_2O$	[O]CO	OCHO	[O]C=O
$CH_3C(O)O$	CC([O])=O	HSO_2	O=[SH]=O
HOS	O[S]	Sa[c]	[S][d]
HSS[b,c]	S=[SH]	HSSH[c]	SS
CH_2SH	[CH]S	HCCS	[S]C#C
H_2SS	S = [SH]	NCN	[N]=C=[N]
CH_2N_2	[CH]N=[N]	H_2CN[b,c]	C=[N]
cNCN	C1=NN=1	CH_2NCN	[CH]N=C=[N]
CH_2NH[b,c]	C=N	NCOH	OC#N
NNH[b,c]	[N]=N	CH_3NH[c]	C[NH]
CH_2NNH	[CH]N=N	CH_2NNH_2	NN=C
CH_2NH_2[b,c]	[CH]N	CHNH	[CH]=N

Notes
[a] Simplified Molecular-Input Line-Entry System.
[b] Species included in VULCAN (Tsai et al. 2017, 2021).
[c] Species included in KINETICS (Moses et al. 2011).
[d] Despite appearing as doublet or triplet radicals in the SMILES representation, these species are singlets in the "adjacency lists" representation, indicating that all electrons are paired.

photochemical kinetic-transport modeling after the treatment described in Yang & Hu (2024).

Among the 92 species, 36 species are newly generated by RMG and not available in the EPACRIS library. When compared to other well-known photochemical networks used for exoplanetary species, within these 36 newly generated species by RMG, 27 species were not included in KINETICS (Moses et al. 2011), and 30 species were not included in VULCAN (Tsai et al. 2017, 2021; see Table C1 for details). Among these not-included species, hydroxymethylene (HCOH) is shown to be a major intermediate species for the conversion of CO into methane and water (Yang et al. 2023). Additionally, many hydroxyl group species such as CH_2CHOH, CH_2CH_2OH, HCCOH, CHCHOH, CH_3CH_2OH, and CH_3CHOH participate in the dehydration reactions that link simple molecules into long and complex chains. For this reason, although these molecules may be challenging to detect with current observational techniques, including them in photochemical modeling is essential, as this can potentially lead to the formation of novel species.

To make sure the chemical reaction network generated for the H_2O-rich conditions is also applicable to the $x_{acc} = 0$

scenario (i.e., H_2:H_2O = 100:0), we conducted photochemical modeling of the H_2-dominated K2-18 b atmosphere using the same atomic abundance and the same T–P profile adopted in MODEL 3 of Wogan et al. (2024). As discussed in Section 3.1.1, the predicted mixing ratios of major species such as CO_2, CH_4, H_2O, N_2, CO, NH_3, and SO_2 were almost identical, confirming the robustness of the model results in both the H_2O- and H_2-dominated regimes.

Appendix D
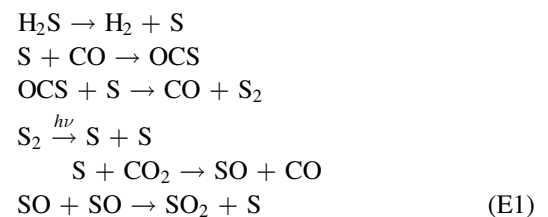## The Eddy Diffusion Coefficients and Stellar Fluxes (Section 2.4)

This appendix provides additional information on the eddy diffusion coefficient profile and stellar fluxes used for 1D photochemical kinetic-transport atmospheric modeling described in Section 2.4

The eddy diffusion coefficient profile was estimated to be a uniform 10^6 [$cm^2 \cdot s^{-1}$] at various altitudes based on Figure 1 in Zhang & Showman (2018). This value is comparable to that of Earth, which ranges from 4×10^3 to 10^6 [$cm^2 \cdot s^{-1}$], and Earth has a planetary equilibrium temperature (T_{eq}) of 255 K, similar to K2-18 b. However, some might argue that K_{zz} could be much smaller, especially if a short-wavelength absorber causes a temperature inversion, as it is in Earth's stratosphere. To test the sensitivity of the steady-state vertical mixing ratios to changes in the eddy diffusion coefficients, we conducted additional modelings with coefficients set at 10^4 and 10^8 [$cm^2 \cdot s^{-1}$] in selected cases. These tests showed that the results were not highly sensitive to variations in the eddy diffusion coefficient, which will be discussed again later.

For simulations involving K2-18 (classified as an M2.8-type star by Montet et al. 2015) and LP 791-18 (classified as an M6-type star by Crossfield et al. 2019), we scaled for the bolometric luminosity using the M5-type stellar spectrum of GJ 876 from the MUSCLES survey III (Loyd et al. 2016). For simulations involving TOI-270 (classified as an M3V-type star by Günther et al. 2019), the M3V-type stellar spectrum of GJ 644 from the same survey was used for the bolometric luminosity scaling.

Appendix E
Details of SO_2 Formation Regimes (Section 3.1.2)

In the regimes with less than approximately $\sim$20% H_2O abundance inside the envelope, SO_2 forms through the following reactions at $P \sim 10$ mbar:

$$H_2S \rightarrow H_2 + S$$
$$S + CO \rightarrow OCS$$
$$OCS + S \rightarrow CO + S_2$$
$$S_2 \xrightarrow{h\nu} S + S$$
$$S + CO_2 \rightarrow SO + CO$$
$$SO + SO \rightarrow SO_2 + S \qquad (E1)$$

In this regime, CO_2 acts as an oxidizer for sulfur due to its thermochemical instability as a carbon-bearing form (with CH_4 being more favorable). Thus, the amount of SO_2 formed is determined by the amount of CO_2 (see mixing ratio patterns at deep interior $H_2O/H_2 \leqslant 0.4$ in both CO_2 and SO_2 panels of Figure 2). Additional SO_2 formation occurs in the upper

atmosphere via photochemistry:

$$H_2O \xrightarrow{h\nu} H + OH$$
$$S + OH \rightarrow SO + H$$
$$SO + OH \rightarrow SO_2 + H. \tag{E2}$$
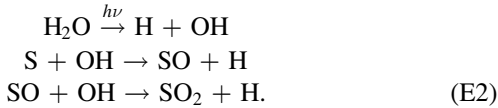
This is the proposed photochemical formation pathway for SO_2 in the hot-Jupiter-type exoplanet WASP-39 b (Tsai et al. 2023).

The transition region between the $\leqslant 20\%$ H_2O region and the $\geqslant 20\%$ region turned out to be very sensitive to the T–P structure of the planet. For example, when comparing the $100 \times Z_\odot$ scenario of K2-18 b assuming $T_{int} = 60$ K and 100 K, there is more than a 6 orders of magnitude difference between the predicted SO_2 mixing ratios. This difference primarily arises from water condensation, which impacts the stability of H_2S, the main precursor for sulfur-bearing species such as SO_2 and OCS. In the scenario where $T_{int} = 100$ K, the deep interior at 100 bars is approximately 250 K hotter compared to the interior assuming $T_{int} = 60$ K. At pressures lower than approximately 3 bars, the entire T–P profile assuming $T_{int} = 100$ K is about 5 K higher compared to the T–P profile assuming $T_{int} = 60$ K. This small difference of about 5 K results in about 15% more H_2O abundance at $P \leqslant \sim 3$ bars for the H_2-dominated atmosphere of K2-18 b assuming $T_{int} = 100$ K, compared to when assuming $T_{int} = 60$ K. This 15% excess H_2O favors the retention of H_2S through the reaction

$$H_2O + SH \rightarrow H_2S + OH. \tag{E3}$$
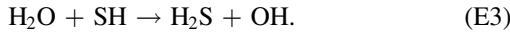
As a result, in the case of H_2-dominated K2-18 b assuming $T_{int} = 100$ K, H_2S can remain stable up to $P \sim 0.2$ mbar, where H_2S photodissociates to form various sulfur-bearing species including SO_2. In contrast, with $T_{int} = 60$ K, H_2S already starts to thermally dissociate into sulfur-bearing species at $P \sim 30$ mbar. This results in significant differences between the predicted SO_2 mixing ratios, as shown in the SO_2 panels of Figure 2. This is also consistent with the OCS case, as evidenced by the rapid decrease of the OCS mixing ratio within this transition region (see blue crosses and blue hexagrams near $100 \times Z_\odot$ gray dotted line in Figure 2). This T–P structure-sensitive behavior of SO_2 driven by H_2O condensation implies that the detection of SO_2 in temperate sub-Neptunes with an internal H_2O envelope of less than 20% may be inconsistent with a high intrinsic temperature (T_{int}).

In the H_2O-rich regime (more than approximately 20% H_2O abundance inside the envelope), SO_2 becomes thermochemically favorable in an oxidizing deep interior. For this reason, SO_2 already exists in significant amounts—up to 100 ppm—in the deep interior and is transported to the upper layers. In the upper atmosphere, additional SO_2 is formed through Scheme E2. Although the vertical mixing ratio of SO_2 varies depending on the eddy diffusion coefficients used in the model and cannot solely represent the predicted SO_2 amount in the observable regime (i.e., $P \sim 1$ mbar) shown in Figure 2, our model indicates that the thermochemical formation of SO_2 in the deep interior contributes significantly to the SO_2 abundance if the interior is water-rich. In these conditions, SO_2 becomes

abundant with higher water content and deep interior temperatures. As shown in Figure 2, SO_2 formation correlates positively with deep interior temperature and the planetary envelope O/H ratio (i.e., H_2O/H_2). For instance, the deep interior temperature tends to increase with the planetary equilibrium temperature. Thus, K2-18 b has the lowest equilibrium temperature at 255 K, followed by LP 791-18 c (324 K), TOI-270 d (354 K), and TOI-270 d assuming $A_b = 0$ with the highest equilibrium temperature of 387 K. A higher [C + N + S] abundance also promotes SO_2 formation.

Appendix F
Details of Sulfur Chemistry in the Atmosphere of K2-18 b
(Section 3.2.1)

The summarized Scheme 1 for the deep interior OCS formation is consistent with the similar vertical mixing ratio profile shape between OCS and CO at $P \geqslant 10^4$ mbar as shown in the left panel of Figure 4. OCS is then transported upward via vertical mixing to the upper atmosphere ($P \leqslant 10$ mbar). In the upper atmosphere, additional OCS forms through a disequilibrium process, primarily driven by UV photochemistry, as follows:

$$H_2S \xrightarrow{h\nu} SH + H$$
$$SH \xrightarrow{h\nu} S + H$$
$$S + CO \xrightarrow{M} OCS, \tag{F1}$$
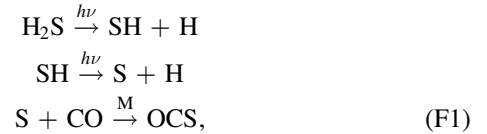
with M representing any third-body molecule. This process aligns with the observed decrease in CO mixing ratios at $P = 10^{-4}$–10^{-2} mbar, above which CO is replenished by CO_2 UV photodissociation. It should be noted that the OCS formation pathways here do not directly involve H_2O or its photolysis. Consequently, the OCS abundance is not sensitive to the condensation of water in the upper atmosphere.

Although sulfur dioxide (SO_2) is also predicted to form at higher altitudes (i.e., $P = 10^{-4}$–10^{-3} mbar) through a similar photochemical scheme described in Tsai et al. (2023), K2-18~b's predicted abundance of SO_2 is insignificant to appear as notable spectral features, compared to the SO_2 spectral feature observed in WASP-39 b (Alderson et al. 2023; Ahrer et al. 2023; Feinstein et al. 2023; Rustamkulov et al. 2023; Powell et al. 2024).

Figure F1 shows the synthesized transmission spectra for K2-18 b (upper panel) and TOI-270 d (bottom panel) based on the dotted lines from Figure 4. Most of the spectral features remain consistent, while the spectral features at ~ 4 μm and 4.8–5 μm change, attributed to SO_2 and OCS. As mentioned in Section 3.2.1 of the main text, the community lacks extensive details on sulfur chemistry, and this strongly suggests the need for future studies to accurately estimate the rate coefficients for sulfur chemistry through both ab initio calculations and experimental reaction kinetic measurements, including Scheme 2 and others, such as S(^{1}D) photochemistry.
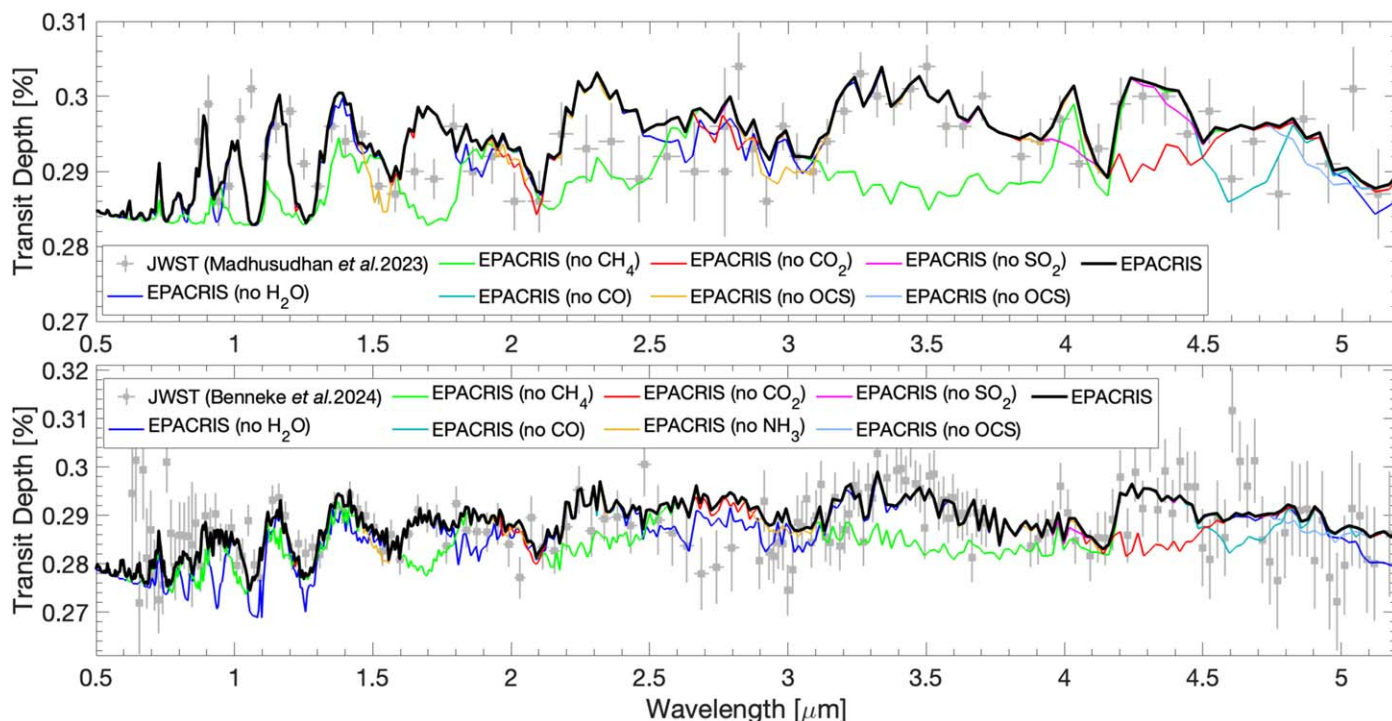
Figure F1. Comparisons between the theoretical transmission spectra generated by EPACRIS (solid lines) and the JWST observations for (top) the $H_2:H_2O = 50:50$ and $[C + N + S] = 100\times$ solar metallicity scenario of K2-18 b assuming $A_b = 0.3$, corresponding to the dotted lines in the left panel of Figure 4, and (bottom) the H_2: $H_2O = 75:25$ and $[C + N + S] = 100\times$ solar metallicity scenario of TOI-270 d assuming $A_b = 0$, corresponding to the dotted lines in the right panel of Figure 4. In this EPACRIS model prediction, the rate coefficient of Scheme 2 is adopted from Tsai et al. (2021), and the major difference from Figure 5 is the amplitude of the SO_2 (significantly increased in the K2-18 b case) and OCS (significantly decreased in the K2-18 b case) features. The gray symbols with error bars indicate JWST observations of the corresponding exoplanets taken from Madhusudhan et al. (2023) for K2-18 b (top) and Benneke et al. (2024) for TOI-270 d (bottom). Each color represents a spectrum generated by excluding specific species: green for no CH_4, red for no CO_2, light blue for no OCS, blue for no H_2O, teal for no CO, light brown for no NH_3, and black for all species included.

ORCID iDs

Jeehyun Yang ● https://orcid.org/0000-0002-1551-2610
Renyu Hu ● https://orcid.org/0000-0003-2215-8485

References

Ahrer, E.-M., Stevenson, K. B., Mansfield, M., et al. 2023, Natur, 614, 653
Alderson, L., Wakeford, H. R., Alam, M. K., et al. 2023, Natur, 614, 664
Benneke, B., Wong, I., Piaulet, C., et al. 2019, ApJL, 887, L14
Benneke, B., Roy, P.-A., Coulombe, L.-P., et al. 2024, arXiv:2403.03325
Brande, J., Crossfield, I. J. M., Kreidberg, L., et al. 2024, ApJL, 961, L23
Buck, A. L. 1981, JApMC, 20, 1527
Burn, R., Mordasini, C., Mishra, L., et al. 2024, NatAs, 8, 463
Cronin, T. W. 2014, JAtS, 71, 2994
Crossfield, I. J. M., Waalkes, W., Newton, E. R., et al. 2019, ApJL, 883, L16
Feinstein, A. D., Radica, M., Welbanks, L., et al. 2023, Natur, 614, 670
Fortney, J. J., Visscher, C., Marley, M. S., et al. 2020, AJ, 160, 288
Fulton, B. J., & Petigura, E. A. 2018, AJ, 156, 264
Fulton, B. J., Petigura, E. A., Howard, A. W., et al. 2017, AJ, 154, 109
Gao, C. W., Allen, J. W., Green, W. H., & West, R. H. 2016, CoPhC, 203, 212
Graham, R. J., Lichtenberg, T., Boukrouche, R., & Pierrehumbert, R. T. 2021, PSJ, 2, 207
Günther, M. N., Pozuelos, F. J., Dittmann, J. A., et al. 2019, NatAs, 3, 1099
Hardegree-Ullman, K. K., Cushing, M. C., Muirhead, P. S., & Christiansen, J. L. 2019, AJ, 158, 75
Heng, K., & Marley, M. S. 2018, Handbook of Exoplanets (Cham: Springer), 2137
Hu, R. 2019, ApJ, 887, 166
Hu, R. 2021, ApJ, 921, 27
Hu, R., Damiano, M., Scheucher, M., et al. 2021, ApJL, 921, L8
Hu, R., & Seager, S. 2014, ApJ, 784, 63
Hu, R., Seager, S., & Bains, W. 2012, ApJ, 761, 166
Hu, R., Seager, S., & Bains, W. 2013, ApJ, 769, 6
Innes, H., Tsai, S.-M., & Pierrehumbert, R. T. 2023, ApJ, 953, 168

Johansen, A., & Lambrechts, M. 2017, AREPS, 45, 359
Johnson, M. S., Dong, X., Grinberg Dana, A., et al. 2022, J Chem Inf Model, 62, 4906
Kempton, E. M.-R., Lessard, M., Malik, M., et al. 2023, ApJ, 953, 57
Lambrechts, M., Johansen, A., & Morbidelli, A. 2014, A&A, 572, A35
Leconte, J., Selsis, F., Hersant, F., & Guillot, T. 2017, A&A, 598, A98
Leconte, J., Spiga, A., Clément, N., et al. 2024, A&A, 686, A131
Line, M. R., Vasisht, G., Chen, P., Angerhausen, D., & Yung, Y. L. 2011, ApJ, 738, 32
Liu, M., Grinberg Dana, A., Johnson, M. S., et al. 2021, J Chem Inf Model, 61, 2686
Lodders, K. 2020, Solar Elemental Abundances, Oxford Research Encyclopedia of Planetary Science (Oxford: Oxford Univ. Press),
Lodders, K., Palme, H., & Gail, H.-P. 2009, LanB, 4B, 712
Loyd, R. O. P., France, K., Youngblood, A., et al. 2016, ApJ, 824, 102
Luque, R., & Pallé, E. 2022, Sci, 377, 1211
Madhusudhan, N., Piette, A. A. A., & Constantinou, S. 2021, ApJ, 918, 1
Madhusudhan, N., Sarkar, S., Constantinou, S., et al. 2023, ApJL, 956, L13
Miller-Ricci, E., Seager, S., & Sasselov, D. 2008, ApJ, 690, 1056
Montet, B. T., Morton, T. D., Foreman-Mackey, D., et al. 2015, ApJ, 809, 25
Morbidelli, A., Lambrechts, M., Jacobson, S., & Bitsch, B. 2015, Icar, 258, 418
Morley, C. V., Fortney, J. J., Marley, M. S., et al. 2015, ApJ, 815, 110
Moses, J. I., Visscher, C., Fortney, J. J., et al. 2011, ApJ, 737, 15
Moses, J. I., Line, M. R., Visscher, C., et al. 2013, ApJ, 777, 34
Moses, J. I., Marley, M. S., Zahnle, K., et al. 2016, ApJ, 829, 66
NASA's Exoplanet Archive 2024, NASA's Exoplanet Archive, https://exoplanets.nasa.gov/
Oya, M., Shiina, H., Tsuchiya, K., & Matsui, H. 1994, BCSJ, 67, 2311
Peterson, M. S., Benneke, B., Collins, K., et al. 2023, Natur, 617, 701
Pierrehumbert, R. T. 2023, ApJ, 944, 20
Powell, D., Feinstein, A. D., Lee, E. K., et al. 2024, Natur, 626, 979
Ranjan, S., Schwieterman, E. W., Harman, C., et al. 2020, ApJ, 896, 148
RMG 2023, Developers of Reaction Mechanism Generator (RMG) and associated software, v3.2.0, GitHub, https://github.com/ReactionMechanismGenerator
Rogers, L. A., & Seager, S. 2010, ApJ, 716, 1208

Rustamkulov, Z., Sing, D. K., Mukherjee, S., et al. 2023, Natur, 614, 659

Scheucher, M., Wunderlich, F., Grenfell, J. L., et al. 2020, ApJ, 898, 44

Shorttle, O., Jordan, S., Nicholls, H., Lichtenberg, T., & Bower, D. J. 2024, ApJL, 962, L8

Sing, D. K., Rustamkulov, Z., Thorngren, D. P., et al. 2024, Natur, 630, 831

Thorngren, D., & Fortney, J. J. 2019, ApJL, 874, L31

Thorngren, D. P., Fortney, J. J., Murray-Clay, R. A., & Lopez, E. D. 2016, ApJ, 831, 64

Tsai, S.-M., Kitzmann, D., Lyons, J. R., et al. 2018, ApJ, 862, 31

Tsai, S.-M., Lyons, J. R., Grosheintz, L., et al. 2017, ApJS, 228, 20

Tsai, S.-M., Malik, M., Kitzmann, D., et al. 2021, ApJ, 923, 264

Tsai, S.-M., Lee, E. K. H., Powell, D., et al. 2023, Natur, 617, 483

Valencia, D., Ikoma, M., Guillot, T., & Nettelmann, N. 2010, A&A, 516, A20

Van Eylen, V., Agentoft, C., Lundkvist, M. S., et al. 2018, MNRAS, 479, 4786

Venot, O., Hébrard, E., Agundez, M., et al. 2012, A&A, 546, A43

Venturini, J., Guilera, O. M., Haldemann, J., Ronco, M. P., & Mordasini, C. 2020, A&A, 643, L1

Welbanks, L., Bell, T. J., Beatty, T. G., et al. 2024, Natur, 630, 836

Wogan, N. F., Batalha, N. E., Zahnle, K., et al. 2024, ApJL, 963, L7

Woiki, D., & Roth, P. 1995, Shock Waves @ Marseille II (Berlin: Springer), 53

Yang, J., Gudipati, M. S., Henderson, B. L., & Fleury, B. 2023, ApJ, 947, 26

Yang, J., & Hu, R. 2024, ApJ, 966, 189

Yu, X., Moses, J. I., Fortney, J. J., & Zhang, X. 2021, ApJ, 914, 38

Zahnle, K., Marley, M. S., Morley, C. V., & Moses, J. I. 2016, ApJ, 824, 137

Zhang, X., & Showman, A. P. 2018, ApJ, 866, 1